



HAL
open science

The JWST Early Release Science Program for Direct Observations of Exoplanetary Systems I: High-Contrast Imaging of the Exoplanet HIP 65426 b from 2–16 μm

Aarynn Carter, Sasha Hinkley, Jens Kammerer, Andrew Skemer, Beth Biller, Jarron Leisenring, Maxwell Millar-Blanchaer, Simon Petrus, Jordan Stone, Kimberly Ward-Duong, et al.

► To cite this version:

Aarynn Carter, Sasha Hinkley, Jens Kammerer, Andrew Skemer, Beth Biller, et al.. The JWST Early Release Science Program for Direct Observations of Exoplanetary Systems I: High-Contrast Imaging of the Exoplanet HIP 65426 b from 2–16 μm . The Astrophysical journal letters, 2023, 951 (1), pp.L20. 10.3847/2041-8213/acd93e . hal-04208380

HAL Id: hal-04208380

<https://hal.science/hal-04208380v1>

Submitted on 15 Sep 2023

HAL is a multi-disciplinary open access archive for the deposit and dissemination of scientific research documents, whether they are published or not. The documents may come from teaching and research institutions in France or abroad, or from public or private research centers.

L'archive ouverte pluridisciplinaire **HAL**, est destinée au dépôt et à la diffusion de documents scientifiques de niveau recherche, publiés ou non, émanant des établissements d'enseignement et de recherche français ou étrangers, des laboratoires publics ou privés.



Distributed under a Creative Commons Attribution 4.0 International License



The JWST Early Release Science Program for Direct Observations of Exoplanetary Systems I: High-contrast Imaging of the Exoplanet HIP 65426 b from 2 to 16 μm

Aarynn L. Carter¹ , Sasha Hinkley² , Jens Kammerer³ , Andrew Skemer¹ , Beth A. Biller⁴ , Jarron M. Leisenring⁵ , Maxwell A. Millar-Blanchaer⁶ , Simon Petrus^{7,8} , Jordan M. Stone⁹ , Kimberly Ward-Duong¹⁰ , Jason J. Wang^{11,12} , Julien H. Girard³ , Dean C. Hines³ , Marshall D. Perrin³ , Laurent Pueyo³, William O. Balmer^{3,13} , Mariangela Bonavita¹⁴ , Mickael Bonnefoy¹⁵ , Gael Chauvin¹⁶ , Elodie Choquet¹⁷ , Valentin Christiaens¹⁸ , Camilla Danielski¹⁹ , Grant M. Kennedy²⁰ , Elisabeth C. Matthews²¹ , Brittany E. Miles¹ , Polychronis Patapis²² , Shrishmoy Ray² , Emily Rickman²³ , Steph Sallum²⁴ , Karl R. Stapelfeldt²⁵ , Niall Whiteford²⁶ , Yifan Zhou²⁷ , Olivier Absil¹⁸ , Anthony Boccaletti²⁸ , Mark Booth²⁹ , Brendan P. Bowler²⁷ , Christine H. Chen^{3,13} , Thayne Currie³⁰ , Jonathan J. Fortney¹ , Carol A. Grady³¹ , Alexandra Z. Greebaum³² , Thomas Henning²¹ , Kielan K. W. Hoch³³ , Markus Janson³⁴ , Paul Kalas^{35,36,37} , Matthew A. Kenworthy³⁸ , Pierre Kervella²⁸ , Adam L. Kraus²⁷ , Pierre-Olivier Lagage³⁹ , Michael C. Liu⁴⁰ , Bruce Macintosh⁴¹ , Sebastian Marino^{42,43} , Mark S. Marley⁴⁴ , Christian Marois⁴⁵ , Brenda C. Matthews⁴⁶ , Dimitri Mawet^{12,25} , Michael W. McElwain⁴⁷ , Stanimir Metchev⁴⁸ , Michael R. Meyer⁴⁹ , Paul Molliere²¹ , Sarah E. Moran⁴⁴ , Caroline V. Morley²⁷ , Sagnick Mukherjee¹ , Eric Pantin⁵⁰ , Andreas Quirrenbach⁵¹ , Isabel Rebollido³ , Bin B. Ren¹⁵ , Glenn Schneider⁵ , Malavika Vasist¹⁸ , Kadin Worthen¹³ , Mark C. Wyatt⁴³ , Zackery W. Briesemeister⁴⁷ , Marta L. Bryan³⁵ , Per Calissendorff⁴⁹ , Faustine Cantalloube¹⁷ , Gabriele Cugno⁴⁹ , Matthew De Furio⁴⁹ , Trent J. Dupuy⁵² , Samuel M. Factor²⁷ , Jacqueline K. Faherty²⁶ , Michael P. Fitzgerald⁵³ , Kyle Franson^{27,61} , Eileen C. Gonzales^{54,62} , Callie E. Hood¹ , Alex R. Howe⁴⁷ , Masayuki Kuzuhara⁵⁵ , Anne-Marie Lagrange²⁸ , Kellen Lawson⁴⁷ , Cecilia Lazzoni² , Ben W. P. Lew⁵⁶ , Pengyu Liu⁴ , Jorge Llop-Sayson¹² , James P. Lloyd⁵⁴ , Raquel A. Martinez²⁴ , Johan Mazoyer²⁸ , Paulina Palma-Bifani¹⁶ , Sascha P. Quanz²² , Jea Adams Redai⁵⁷ , Matthias Samland²¹ , Joshua E. Schlieder⁴⁷ , Motohide Tamura⁵⁸ , Xianyu Tan⁵⁹ , Taichi Uyama³² , Arthur Vigan¹⁷ , Johanna M. Vos^{26,60} , Kevin Wagner^{5,63} , Schuyler G. Wolff⁵ , Marie Ygouf²⁵ , Xi Zhang¹ , Keming Zhang³⁵ , and Zhoujian Zhang²⁷ 

¹ Department of Astronomy & Astrophysics, University of California, Santa Cruz, 1156 High St, Santa Cruz, CA 95064, USA; aarynn.carter@ucsc.edu

² University of Exeter, Astrophysics Group, Physics Building, Stocker Road, Exeter, EX4 4QL, UK

³ Space Telescope Science Institute, 3700 San Martin Drive, Baltimore, MD 21218, USA

⁴ Scottish Universities Physics Alliance, Institute for Astronomy, University of Edinburgh, Blackford Hill, Edinburgh EH9 3HJ, UK; Centre for Exoplanet Science, University of Edinburgh, Edinburgh EH9 3HJ, UK

⁵ Steward Observatory and the Department of Astronomy, The University of Arizona, 933 N Cherry Ave, Tucson, AZ 85721, USA

⁶ Department of Physics, University of California, Santa Barbara, CA 93106, USA

⁷ Instituto de Física y Astronomía, Facultad de Ciencias, Universidad de Valparaíso, Av. Gran Bretaña 1111, Valparaíso, Chile

⁸ Núcleo Milenio Formación Planetaria - NPF, Universidad de Valparaíso, Av. Gran Bretaña 1111, Valparaíso, Chile

⁹ Naval Research Laboratory, Remote Sensing Division, 4555 Overlook Ave SW, Washington, DC 20375, USA

¹⁰ Department of Astronomy, Smith College, Northampton, MA 01063, USA

¹¹ Center for Interdisciplinary Exploration and Research in Astrophysics (CIERA) and Department of Physics and Astronomy, Northwestern University, Evanston, IL 60208, USA

¹² Department of Astronomy, California Institute of Technology, Pasadena, CA 91125, USA

¹³ Department of Physics & Astronomy, Johns Hopkins University, 3400 N. Charles Street, Baltimore, MD 21218, USA

¹⁴ School of Physical Sciences, Faculty of Science, Technology, Engineering and Mathematics, The Open University, Walton Hall, Milton Keynes, MK7 6AA, UK

¹⁵ Université Grenoble Alpes, Institut de Planétologie et d'Astrophysique (IPAG), F-38000 Grenoble, France

¹⁶ Laboratoire J.-L. Lagrange, Université Côte d'Azur, CNRS, Observatoire de la Côte d'Azur, F-06304 Nice, France

¹⁷ Aix Marseille Univ, CNRS, CNES, LAM, Marseille, France

¹⁸ Space sciences, Technologies & Astrophysics Research (STAR) Institute, Université de Liège, Allée du Six Août 19c, B-4000 Sart Tilman, Belgium

¹⁹ Instituto de Astrofísica de Andalucía, CSIC, Glorieta de la Astronomía s/n, E-18008, Granada, Spain

²⁰ Department of Physics, University of Warwick, Gibbet Hill Road, Coventry, CV4 7AL, UK

²¹ Max-Planck-Institut für Astronomie, Königstuhl 17, D-69117 Heidelberg, Germany

²² Institute of Particle Physics and Astrophysics, ETH Zurich, Wolfgang-Pauli-Str. 27, 8093 Zurich, Switzerland

²³ European Space Agency (ESA), ESA Office, Space Telescope Science Institute, 3700 San Martin Drive, Baltimore, MD 21218, USA

²⁴ Department of Physics and Astronomy, 4129 Frederick Reines Hall, University of California, Irvine, CA 92697, USA

²⁵ Jet Propulsion Laboratory, California Institute of Technology, 4800 Oak Grove Drive, Pasadena, CA 91109, USA

²⁶ Department of Astrophysics, American Museum of Natural History, Central Park West at 79th Street, NY 10024, USA

²⁷ Department of Astronomy, University of Texas at Austin, 2515 Speedway Stop C1400, Austin, TX 78712, USA

²⁸ LESIA, Observatoire de Paris, Université PSL, CNRS, Université Paris Cité, Sorbonne Université, 5 place Jules Janssen, F-92195 Meudon, France

²⁹ Astrophysikalisches Institut und Universitätssternwarte, Friedrich-Schiller-Universität Jena, Schillergäßchen 2-3, D-07745 Jena, Germany

³⁰ Department of Physics and Astronomy, University of Texas-San Antonio, 1 UTSA Circle, San Antonio, TX, USA; Subaru Telescope, National Astronomical Observatory of Japan, 650 North A'ohōkū Place, Hilo, HI 96720, USA

³¹ Eureka Scientific, 2452 Delmer St., Suite 1, Oakland CA, 96402, USA

³² IPAC, California Institute of Technology, 1200 E. California Blvd., Pasadena, CA 91125, USA

³³ Center for Astrophysics and Space Sciences, University of California, San Diego, La Jolla, CA 92093, USA

³⁴ Department of Astronomy, Stockholm University, AlbaNova University Center, SE-10691 Stockholm, Sweden

³⁵ Department of Astronomy, 501 Campbell Hall, University of California Berkeley, Berkeley, CA 94720-3411, USA

³⁶ SETI Institute, Carl Sagan Center, 189 Bernardo Ave., Mountain View CA 94043, USA

³⁷ Institute of Astrophysics, FORTH, GR-71110 Heraklion, Greece

³⁸ Leiden Observatory, Leiden University, P.O. Box 9513, 2300 RA Leiden, The Netherlands

³⁹ Université Paris-Saclay, Université Paris Cité, CEA, CNRS, AIM, F-91191, Gif-sur-Yvette, France

⁴⁰ Institute for Astronomy, University of Hawai'i, 2680 Woodlawn Drive, Honolulu HI 96822, USA⁴¹ Kavli Institute for Particle Astrophysics and Cosmology, Stanford University, Stanford, CA 94305, USA⁴² Jesus College, University of Cambridge, Jesus Lane, Cambridge CB5 8BL, UK⁴³ Institute of Astronomy, University of Cambridge, Madingley Road, Cambridge CB3 0HA, UK⁴⁴ Dept. of Planetary Sciences; Lunar & Planetary Laboratory; Univ. of Arizona; Tucson, AZ 85721, USA⁴⁵ National Research Council of Canada, Canada⁴⁶ Herzberg Astronomy & Astrophysics Research Centre, National Research Council of Canada, 5071 West Saanich Road, Victoria, BC V9E 2E7, Canada⁴⁷ NASA-Goddard Space Flight Center, 8800 Greenbelt Rd, Greenbelt, MD 20771, USA⁴⁸ Western University, Department of Physics & Astronomy and Institute for Earth and Space Exploration, 1151 Richmond Street, London, Ontario N6A 3K7, Canada⁴⁹ Department of Astronomy, University of Michigan, 1085 S. University, Ann Arbor, MI 48109, USA⁵⁰ IRFU/DAP Département D'Astrophysique CE Saclay, Gif-sur-Yvette, France⁵¹ Landessternwarte, Zentrum für Astronomie der Universität Heidelberg, Königstuhl 12, D-69117 Heidelberg, Germany⁵² Institute for Astronomy, University of Edinburgh, Royal Observatory, Blackford Hill, Edinburgh, EH9 3HJ, UK⁵³ University of California, Los Angeles, 430 Portola Plaza Box 951547, Los Angeles, CA 90095-1547, USA⁵⁴ Department of Astronomy and Carl Sagan Institute, Cornell University, 122 Sciences Drive, Ithaca, NY 14853, USA⁵⁵ Astrobiology Center of NINS, 2-21-1, Osawa, Mitaka, Tokyo, 181-8588, Japan⁵⁶ Bay Area Environmental Research Institute and NASA Ames Research Center, Moffett Field, CA 94035, USA⁵⁷ Center for Astrophysics | Harvard & Smithsonian, 60 Garden Street, Cambridge, MA 02138, USA⁵⁸ The University of Tokyo, 7-3-1 Hongo, Bunkyo-ku, Tokyo 113-0033, Japan⁵⁹ Atmospheric, Ocean, and Planetary Physics, Department of Physics, University of Oxford, UK⁶⁰ Dublin Institute for Advanced Studies, School of Cosmic Physics, 31 Fitzwilliam Place, Dublin 2, D02 XF86, Ireland

Received 2022 August 31; revised 2023 April 28; accepted 2023 May 19; published 2023 July 6

Abstract

We present JWST Early Release Science coronagraphic observations of the super-Jupiter exoplanet, HIP 65426b, with the Near-Infrared Camera (NIRCam) from 2 to 5 μm , and with the Mid-Infrared Instrument (MIRI) from 11 to 16 μm . At a separation of $\sim 0''.82$ (87_{-31}^{+108} au), HIP 65426b is clearly detected in all seven of our observational filters, representing the first images of an exoplanet to be obtained by JWST, and the first-ever direct detection of an exoplanet beyond 5 μm . These observations demonstrate that JWST is exceeding its nominal predicted performance by up to a factor of 10, depending on separation and subtraction method, with measured 5σ contrast limits of $\sim 1 \times 10^{-5}$ and $\sim 2 \times 10^{-4}$ at 1'' for NIRCam at 4.4 μm and MIRI at 11.3 μm , respectively. These contrast limits provide sensitivity to sub-Jupiter companions with masses as low as $0.3M_{\text{Jup}}$ beyond separations of ~ 100 au. Together with existing ground-based near-infrared data, the JWST photometry are fit well by a BT-SETTL atmospheric model from 1 to 16 μm , and they span $\sim 97\%$ of HIP 65426b's luminous range. Independent of the choice of model atmosphere, we measure an empirical bolometric luminosity that is tightly constrained between $\log(L_{\text{bol}}/L_{\odot}) = -4.31$ and -4.14 , which in turn provides a robust mass constraint of $7.1 \pm 1.2 M_{\text{Jup}}$. In totality, these observations confirm that JWST presents a powerful and exciting opportunity to characterize the population of exoplanets amenable to high-contrast imaging in greater detail.

Unified Astronomy Thesaurus concepts: [Exoplanets \(498\)](#); [Exoplanet astronomy \(486\)](#); [Extrasolar gaseous planets \(2172\)](#)

1. Introduction

Across the last 25 years, a variety of observational techniques have been employed to uncover and characterize the current population of over 5000 confirmed exoplanets (NASA Exoplanet Science Institute 2020). Of these techniques, the direct detection of photons from an exoplanetary atmosphere—direct imaging—remains one of the most challenging due to the substantial contrast in flux between host stars and their exoplanetary companions. The emitted flux of an exoplanet can be many magnitudes fainter than the stellar diffraction halo at its angular separation, and bespoke instrumentation (e.g., Macintosh et al. 2014; Beuzit et al. 2019) and/or image post-processing (e.g., Chauvin et al. 2004; Marois et al. 2008) are needed to isolate the exoplanet

emission. Even with state-of-the-art instruments and data analysis procedures, only ~ 20 planetary-mass companions (PMCs) have been detected and characterized through these “high-contrast” observations (Currie et al. 2022), and all exoplanets directly imaged to date have estimated or dynamically measured masses $\gtrsim 2 M_{\text{Jup}}$.

Despite these drawbacks, high-contrast observations offer considerable advantages to other techniques. At present, high-contrast imaging is the most viable technique for characterizing the population of exoplanets at orbital separations greater than ~ 10 au. Furthermore, beyond the large population of irradiated, close-in planets with atmospheric measurements obtained via exoplanet transit observations, direct observations of exoplanet emission remain the most readily accessible path toward the characterization of exoplanet atmospheres. Constraints on atmospheric composition may improve our understanding of exoplanet formation and evolution (e.g., Öberg et al. 2011; Morley et al. 2019; Zhang et al. 2021; Mollière et al. 2022), although these determinations can be highly dependent on the post-formation accretion of solid material. Compared to close-in transiting exoplanets, directly imaged planets present a distinct advantage in this regard, as they are easier to detect at younger ages, where they are less likely to have experienced

⁶¹ NSF Graduate Research Fellow.⁶² 51 Pegasi b Fellow.⁶³ NASA Hubble Fellowship Program Sagan Fellow.

significant migration and/or accretion. Additionally, at young ages, bulk properties such as temperature, radius, and bolometric luminosity provide independent constraints on formation conditions (Marley et al. 2007; Marleau & Cumming 2014) that can be contrasted with atmosphere-driven conclusions on formation. Finally, the study of exoplanet atmospheres continues to advance toward smaller and more Earth-like exoplanets, and it could ultimately lead to the discovery of life outside our Solar System (Schwieterman et al. 2018).

Nevertheless, to fully realize the advantages of high-contrast imaging, upgraded or new observatories and instruments (e.g., Gardner et al. 2006; Males et al. 2018; Chilcote et al. 2020) will be necessary so that we can expand this technique across a broader wavelength range, and to a wider diversity of closer separation and/or lower-mass exoplanets.

1.1. High-contrast Observations with JWST

With a primary mirror diameter of 6.5 m, an operational wavelength range from 0.6 to 28.1 μm , and a diverse range of instrumental modes, JWST (Gardner et al. 2006) presents a revolutionary opportunity for scientific exploration and discovery across many branches of astronomy and astrophysics. Within this remit, high-contrast observations of exoplanets and exoplanetary systems are no exception.

JWST is located at the second Sun–Earth Lagrange point, far from the thermal background, telluric contamination, and wave front aberrations generated by Earth’s atmosphere. The combination of excellent optical performance (~ 75 – 130 nm rms wave front error, depending on the instrument), highly stable wave front (< 2 nm drift over a few hours), and large telescope aperture enables JWST to reach better photometric and spectroscopic limiting sensitivities than both past and current ground- (i.e., 8–10 m class telescopes) and space-based (e.g., Hubble, Spitzer) observatories (Rigby et al. 2023). It is not only this increased sensitivity that improves our ability to detect and characterize faint objects such as exoplanets, but its combination with JWST’s access to the near- and mid-infrared. At these wavelengths, the flux emitted from a hotter host star steadily decreases as a function of increasing wavelength, whereas the flux emitted from cooler exoplanetary companions reaches a peak. Hence, the natural star–planet contrast is minimized. To realize these advantages, JWST offers a selection of instrumental modes designed for, or that can be applied to, high-contrast observations. Specifically, both NIRCам (Rieke et al. 2005) and MIRI (Rieke et al. 2015) are equipped with coronagraphic masks (Krist et al. 2009; Boccaletti et al. 2015), NIRISS (Doyon et al. 2012) is equipped with a non-redundant mask that enables aperture masking interferometry (AMI; Sivaramakrishnan et al. 2012), and although lacking any hardware for starlight suppression, both NIRSspec (Bagnasco et al. 2007) and MIRI are equipped with integral field units (IFUs; Wells et al. 2015; Böker et al. 2022).

In anticipation of the range of capabilities that JWST would provide, a similar range of predictions and simulations were constructed in an effort to forecast its potential for exoplanet imaging science. With JWST’s extraordinary sensitivity across 4– $15\mu\text{m}$ (where cooler planets are more luminous; Morley et al. 2014), the first direct detections of sub-Jupiter, and even sub-Saturn, mass planets will be within reach (Beichman et al. 2020; Brande et al. 2020; Carter et al. 2021a; Ray et al. 2023).

Already discovered companions will also be readily detectable across this broad wavelength range, allowing for deeper atmospheric characterizations that may result in the detection of a range of atmospheric species (Danielski et al. 2018; Patapis et al. 2022), or tighter constraints on bulk planetary properties.

Nevertheless, these predictions are based on ground-based testing and observatory simulations, whereas the true capabilities of JWST hinge on its on-sky performance. Preliminarily, the performance of both the NIRCам and MIRI coronagraphic modes exceeded expectations during observatory commissioning (Boccaletti et al. 2022; Girard et al. 2022; Kammerer et al. 2022), but the first scientific demonstrations of JWST’s capabilities are being conducted as part of the Director’s Discretionary Early Release Science (ERS) Programs.⁶⁴

Our ERS program “High Contrast Imaging of Exoplanets and Exoplanetary Systems with JWST” (ERS-01386; Hinkley et al. 2022) is the only ERS program that has tested the high-contrast exoplanet imaging modes of JWST and includes coronagraphic imaging from 2 to 16 μm of the known exoplanet HIP 65426b (Chauvin et al. 2017; this work) and circumstellar disk HD 141569 A (Weinberger et al. 1999; M. Millar-Blanchaer et al. 2023, in preparation; E. Choquet et al. 2023, in preparation), spectroscopy from 1 to 28 μm of the PMC VHS J125601.92-125723.9 AB b (VHS 1256b; Gauza et al. 2015; Miles et al. 2023), and AMI observations of HIP 65426 at 3.8 μm (S. Sallum et al. 2023, in preparation; S. Ray et al. 2023, in preparation). This program is rapidly disseminating these crucial initial data, and it is demonstrating the true capabilities of JWST for high-contrast imaging and spectroscopy for the first time. Furthermore, we will provide a range of science enabling products (e.g., data analysis pipelines and recommendations for best observing practices) to the community, to support their own proposals and investigations in Cycle 2 and beyond (Hinkley et al. 2022).

In this work, we focus exclusively on the coronagraphic imaging observations of the HIP 65426 system within this ERS program, and their context within a broader understanding of JWST as a tool for high-contrast imaging.

1.2. HIP 65426b

Discovered by Chauvin et al. (2017), HIP 65426b is a super-Jupiter-mass exoplanet at a wide physical separation of 110_{-30}^{+90} au (Cheetham et al. 2019) to the star HIP 65426 (A2V, $2M_{\text{J}}$, $J-K = 0.055$, $M_{\odot} = 1.96 \pm 0.04$). HIP 65426 is located at a distance of 107.49 ± 0.40 pc (Gaia Collaboration 2021), has no signs of binarity from radial velocity and sparse aperture masking observations (Chauvin et al. 2017; Cheetham et al. 2019), and it is a fast rotator ($v \sin(i) = 299 \pm 9$ km s⁻¹, Chauvin et al. 2017). Furthermore, HIP 65426 is a likely member of the Lower Centaurus–Crux association as derived from its proper motion and radial velocity measurements (89% probability, Gagné et al. 2018), constraining its age to 14 ± 4 Myr. The interest in this association has grown over time with the increasing number of directly imaged exoplanet discoveries within it, e.g., HD 95086b (Rameau et al. 2013), PDS 70 b/c (Keppler et al. 2018), and TYC 8998b/c (Bohn et al. 2020).

Although HIP 65426b was initially observed with a combination of low-resolution spectroscopy and photometry

⁶⁴ <https://www.stsci.edu/jwst/science-execution/approved-ers-programs>

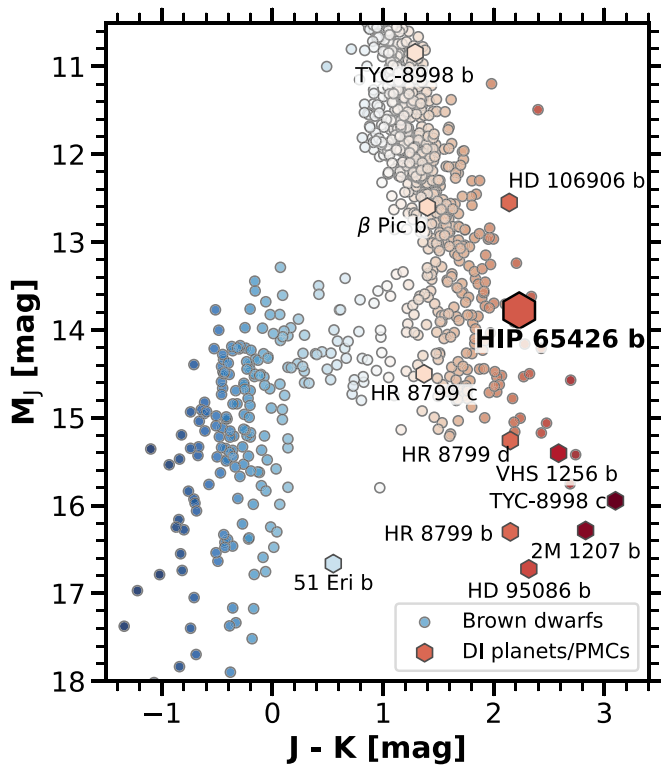


Figure 1. Color-magnitude diagram showing the position of HIP 65426b (Chauvin et al. 2017) relative to both the population of brown dwarf objects (circles) and a selection of directly imaged planetary-mass companions (PMCs, hexagons), as obtained from Best et al. (2020).

from ~ 1 to $2 \mu\text{m}$ (Chauvin et al. 2017), follow-up observations expanded this coverage to $\sim 1\text{--}5 \mu\text{m}$ (Cheetham et al. 2019; Stolker et al. 2020b), including a medium-resolution spectrum from ~ 2 to $2.5 \mu\text{m}$ ($R \simeq 5500$, Petrus et al. 2021). Photometric analysis has demonstrated that HIP 65426b is located similarly to mid-to-late L-dwarfs in color-magnitude diagrams (Figure 1), and it lies between already discovered early L-dwarf exoplanet companions (e.g., β Pic b, HD 106906b) and those at the L/T transition (e.g., HR 8799c/d/e). Using combined photometric and spectroscopic observations, Petrus et al. (2021) performed an atmospheric forward model analysis of HIP 65426b, indicating that it has $T_{\text{eff}} = 1560 \pm 100 \text{ K}$, $\log(g) \leq 4.40 \text{ dex}$ and $[M/H] = 0.05_{-0.22}^{+0.24} \text{ dex}$, and the atmospheric carbon-to-oxygen ratio has an upper limit of $C/O \leq 0.55$. Furthermore, Petrus et al. (2021) also detect the presence of H_2O and CO in the atmosphere of HIP 65426b using cross-correlation molecular mapping, in addition to nondetections of CH_4 and NH_3 . Finally, from evolutionary model analyses to the data reported in Chauvin et al. (2017), Marleau et al. (2019) estimate the mass of HIP 65426b to be $9.9_{-1.8}^{+1.1} M_{\text{Jup}}$ or $10.9_{-2.0}^{+1.4} M_{\text{Jup}}$ for hot- or cold-start initial entropy conditions, respectively (see, e.g., Marley et al. 2007; Spiegel & Burrows 2012).

In Section 2, we describe our JWST observations of HIP 65426b and all necessary data reduction. In Section 3, we describe the analysis steps taken to produce residual starlight subtracted images and measurements of contrast performance. We present a discussion of these observations in the context of both the overall performance of JWST in Section 4, and our understanding of HIP 65426b in Section 5. Finally, we summarize our conclusions in Section 6.

2. Observations and Data Reduction

The NIRCcam and MIRI coronagraphic imaging observations of HIP 65426b presented here were taken as part of program ERS-01386 (Hinkley et al. 2022) and exist as a subset of a broad range of observations to assess the performance of JWST’s high-contrast imaging and spectroscopic modes with respect to the study of exoplanetary systems (Hinkley et al. 2022).

2.1. Observational Structure

The observational strategies used for this program were adopted following the recommended best practices as known prior to launch and described in the JWST user documentation.^{65,66} All observations of HIP 65426b are repeated at two independent roll angles separated by $\sim 10^\circ$ to enable subtraction of the residual stellar point-spread function (PSF) through angular differential imaging (ADI; Müller & Weigelt 1985; Liu 2004; Marois et al. 2006). Although a large number of rolls across a larger angular range would be desirable for an optimal subtraction using this technique, the combination of lengthy exposure times, increased overheads, and spacecraft orientation constraints prohibit an observing strategy more complex than described. Given the maximum possible roll offset for JWST at any given epoch is 14° , a larger roll offset than we have adopted would also require multi-epoch observations.

We also perform similar observations of a bright reference star, HIP 68245 (B2IV, 2MASS $J = 4.628$, $J-K = 0.137$), to additionally enable subtraction through reference differential imaging (RDI). This star was selected because (a) it is bright, therefore reducing the exposure time required to attain a signal-to-noise ratio similar to that of the science target; (b) it has a spectral type similar to that of the science target, therefore reducing the impact of spectral type mismatch; (c) it is relatively close ($\sim 10^\circ$) to the science target, therefore reducing slew overheads and minimizing position-dependent wave front drift between science and reference observations; and (d) it has no evidence of binarity as determined by VLT/SPHERE AMI observations (Proposal ID: 108.22CD). For information on selecting a suitable reference star, see the JWST User Documentation.⁶⁷ All exposure settings for the science and reference observations are shown in Table 1.

An RDI-based subtraction is likely to reach contrast limits superior to those of ADI from prelaunch predictions (Lajoie et al. 2016; Perrin et al. 2018; Carter et al. 2021b), and it is therefore also more representative of the optimal performance of JWST coronagraphy (also see Section 4.1). The exposure settings for these reference observations were chosen to reach an approximately equivalent fraction of full well saturation per integration as the corresponding target observations. Additionally, each reference observation was repeated at nine separate dither positions following small-grid dither patterns 9-POINT-CIRCLE and 9-POINT-SMALL-GRID for the NIRCcam and MIRI observations, respectively (Soummer et al. 2014; Lajoie et al. 2016). The goal of this strategy is to produce a small

⁶⁵ <https://jwst-docs.stsci.edu/jwst-near-infrared-camera/nircam-observing-strategies/nircam-coronagraphic-imaging-recommended-strategies>

⁶⁶ <https://jwst-docs.stsci.edu/jwst-mid-infrared-instrument/miri-observing-strategies/miri-coronagraphic-recommended-strategies>

⁶⁷ <https://jwst-docs.stsci.edu/methods-and-roadmaps/jwst-high-contrast-imaging/jwst-high-contrast-imaging-proposal-planning/hci-psf-reference-stars>

Table 1
Target and Reference Exposure Settings

Filter	λ_{mean} (μm)	W_{eff} (μm)	Mask	Readout	N_{groups}	N_{ints}	t_{exp} (s)	N_{dithers}	N_{rolls}	t_{total} (s)
HIP 65426										
F250M	2.523	0.179	MASK335R	DEEP8	15	4	1235.892	1	2	2471.784
F300M	3.067	0.325	MASK335R	DEEP8	15	4	1235.892	1	2	2471.784
F356W	3.580	0.769	MASK335R	DEEP8	15	2	617.946	1	2	1235.892
F410M	4.084	0.436	MASK335R	DEEP8	15	2	617.946	1	2	1235.892
F444W	4.397	0.979	MASK335R	DEEP8	15	2	617.946	1	2	1235.892
F1140C	11.307	0.608	FQPM1140	FASTR1	101	41	1002.102	1	2	2004.204
F1550C	15.514	0.703	FQPM1550	FASTR1	250	60	3609.341	1	2	7218.682
HIP 68245										
F250M	2.523	0.179	MASK335R	MEDIUM8	4	4	166.852	9	1	1501.669
F300M	3.067	0.325	MASK335R	MEDIUM8	4	4	166.852	9	1	1501.669
F356W	3.580	0.769	MASK335R	MEDIUM8	4	2	83.426	9	1	750.835
F410M	4.084	0.436	MASK335R	MEDIUM8	4	2	166.852	9	1	750.835
F444W	4.397	0.979	MASK335R	MEDIUM8	4	2	83.426	9	1	750.835
F1140C	11.307	0.608	FQPM1140	FASTR1	52	10	126.791	9	1	1141.116
F1550C	15.514	0.703	FQPM1550	FASTR1	100	19	459.706	9	1	4137.356

Note. Background observations were also performed for the MIRI F1140C and F1550C filters with parameters identical to two exposures of a single roll or dither of the target and reference observations, respectively (see Section 2.1). Filter mean wavelengths (λ_{mean}) and bandwidths (W_{eff}) are taken from `spaceKLIP` (see Section 2.2). See <https://jwst-docs.stsci.edu/understanding-exposure-times> for further detail on JWST exposure settings.

library of reference PSFs for each science exposure that captures different misalignments between the star and the center of the coronagraphic mask, and can in turn facilitate more advanced PSF subtraction techniques (e.g., KLIP, Soummer et al. 2012). Further discussion on the relative benefits between ADI and RDI subtraction strategies, or a combination of the two, with respect to these JWST observations can be found in Section 4.1.

For MIRI, we also add background observations to both our science and reference observations in both filters of a nearby “empty” region of sky (as identified in WISE images; Wright et al. 2010) separated ~ 1.5 from the target star to measure the stray light “glow stick” that is inherent to MIRI coronagraphic observations (Boccaletti et al. 2022). Specifically, this position corresponds to an R.A. and a decl. of $\alpha = 13^{\circ}24'44''2915$ and $\delta = -51^{\circ}29'31''54$, respectively (ICRS J2000 coordinates). To best match the science and reference observations, the exposure parameters for each background observation exactly match the parameters for a single roll/dither of the associated science or reference target. These observations were intended to be performed at two separate dither positions to identify astrophysical sources that might impact the background subtraction; however, due to a previously unresolved issue, they were instead repeated at an identical pointing (Dean Hines, private communication).

The NIRCcam and MIRI observations were executed as two separate noninterruptible sequences, ensuring that observations between rolls, and also between science, reference, and background targets, are minimally separated in time. This reduces the extent to which the wave front can vary across observations, due to variations in the telescope mirror alignment, the thermal evolution of the telescope, or both (Perrin et al. 2018; Carter et al. 2021b). Changes in the wave front will lead to variations in the residual PSF between exposures, hinder our ability to perform an optimal subtraction of these residual PSFs, and suppress the overall achievable contrast.

2.2. SpaceKLIP

For all observations, we perform data reduction using the newly developed and publicly available Python package, `spaceKLIP`⁶⁸ (Kammerer et al. 2022). Briefly, `spaceKLIP` takes a collection of data products from the `jwst pipeline`^{69,70} (Bushouse et al. 2022) as inputs, and generates PSF subtracted images, contrast curves, and measurements of companion photometry and astrometry. The majority of this functionality is provided by the underlying `pyKLIP` (Wang et al. 2015) package, with `spaceKLIP` providing a user friendly interface, streamlined code execution, custom JWST data reduction routines, and built-in plotting procedures.

2.3. NIRCcam Coronagraphy

The NIRCcam observational sequence was executed from 23:00 July 29th to 05:16 July 30th 2022 UTC, with exposures taken using the MASK335R round coronagraphic mask (Krist et al. 2010) in the F250M, F300M, F410M, F356W, and F444W filters for the reference star (PA = 110°2), then HIP 65426 (PA = 110°0), and then finally HIP 65426 at a second roll angle (PA = 120°4). This sequence structure significantly reduces overheads, as once the target acquisition has been performed, it is not necessary to reacquire the target to switch the observational filter.

We begin data reduction using the Stage 0 (*uncal.fits) files as generated by the `jwst pipeline`. These products are then processed to Stage 1 (*rateints.fits) files using `spaceKLIP`, which follows a slightly modified version of the `jwst pipeline`. Where possible, the JWST detectors have reference pixels that can be used to track and correct drifts in the measured pixel counts due to readout electronics. In the absence of such a reference, these drifts may instead be misinterpreted as “jumps”⁷¹ from

⁶⁸ <https://github.com/kammerje/spaceKLIP>

⁶⁹ <https://jwst-pipeline.readthedocs.io>

⁷⁰ All data were processed using pipeline version, CAL_VAR = 1.9.4, and calibration reference data, CRDS_CTX = jwst_1041.pmap

⁷¹ <https://jwst-pipeline.readthedocs.io/en/latest/jwst/jump/description.html>

cosmic ray events during the up-the-ramp (MULTIACCUM) detector readout. The NIRCcam coronagraphic subarrays do not have any embedded reference pixels, and default pipeline processing leads to multiple erroneous jump detections and greatly increased noise in processed images. Therefore, we manually define all pixels within a four pixel border of each image as reference pixels within the pipeline, to mitigate these effects. Additionally, we identify a significant improvement in image quality by skipping the dark current subtraction step that is turned on as a default in the `jwst` pipeline. At present, the dark current calibration data exhibit a large number of hot pixels, persistence, and cosmic rays that cannot be averaged out or corrected, due to limited number of available integrations. Attempts to perform a dark current subtraction using this data result in a variety of negative flux residuals in the reduced images and an overall reduced sensitivity of the final pipeline product. Once this calibration file is improved through further calibration observations, we do not anticipate a need to skip this step for NIRCcam coronagraphic data.

During the jump detection step, the `jwst` pipeline will make use of a detection threshold value based on the estimated signal and noise to assess whether a deviation between groups is significant enough to be considered a jump (see footnote 6 for further detail). The default value for this threshold is 4, but we repeat an early version of our F444W analysis across thresholds of 4 to 16 to search for potential improvements. We find that the contrast is slightly improved from a threshold of 4 to 5 by $\sim 5 \times 10^{-8}$ at $1''$, but at larger thresholds it does not vary (deviations $< 1 \times 10^{-8}$ at $1''$). Hence, we adopt a detection threshold of 5 for all of our NIRCcam analyses.

The Stage 1 products are processed further to Stage 2 (`*calints.fits`) files using `spaceKLIP`, with some additional pixel cleaning procedures as follows. First, every pixel with a data quality flag (e.g., indicating hot or warm pixels, unreliable data processing) is replaced by the median of its orthogonal and diagonal neighbors, with the notable exclusion of pixels with a jump flag, which are typically grouped in clusters. We also inspect each pixel for temporal flux variations and identify situations where: (a) the pixel is bright ($\text{MJy sr}^{-1} > 1$) for at least one integration and (b) the pixel is relatively faint (a $> 80\%$ decrease in flux compared to the brightest integration) for at least one integration. The pixel values for the integrations that are not marked as faint are then replaced by the median value of the integrations that are marked as faint. We note here that an outlier identification process based on variations from the standard deviation of each pixel in time may be preferable, but this is difficult to incorporate, given the small number of integrations in these exposures (see Table 1). Despite the above corrections, ~ 25 static hot pixels remain across all images. Although these pixels do not impact our ability to recover HIP 65426b, they introduce residuals in the PSF subtraction process (see Section 2.6) that bias our measurements of the contrast performance. Therefore, we provide the locations of these pixels to `spaceKLIP` manually and correct them in an identical manner as for the pixels marked with data quality flags.

As the NIRCcam PSF in the F250M filter is undersampled, ringing artifacts are generated by the interpolation methods in `pyKLIP` used for image registration and spatial shifting of input PSFs. These artifacts bias the image registration process and limit our ability to accurately inject synthetic PSFs for contrast curve calibration and companion astrometry and

photometry. To overcome this issue, we smooth all of the F250M images by a Gaussian filter, as implemented by `scipy`, with $\sigma = 1.3$ pixels. This value of σ was chosen because it was the minimum possible value that removed the observed artifacts across a test of ten equally spaced values from $\sigma = 1$ to $\sigma = 2$. We note that this factor of 1.3 is consistent with the ratio of the detector pixel scale and the theoretical Nyquist sampling at $2.5 \mu\text{m}$ (assuming a reduced primary mirror diameter of 5.2 m due to the NIRCcam Lyot stop). Smoothing these images may lead to reduced precision in our astrometric analysis; however, it should not influence the accuracy of our retrieved photometry.

2.4. MIRI Coronagraphy

The MIRI observational sequence was executed from 21:05 2022 July 17th to 05:19 2022 July 18th UTC. Exposures were taken for HIP 65426 in the F1140C filter (PA = $117^\circ 4$), then once again at a second roll angle (PA = $108^\circ 0$), and then for the reference star (PA = $109^\circ 2$). This sequence was then repeated in reverse for the F1550C filter, except with slightly different target roll angles of $108^\circ 2$ and $117^\circ 4$. This structure is different from that of the NIRCcam observations, as each filter is tied to a specific four-quadrant phase mask coronagraph (FQPM; Boccaletti et al. 2015), and target acquisition must be repeated when switching between them. Inserting the reference observations between the observations of HIP 65426b minimizes the time separation between science and reference exposures for each filter, and therefore the extent of the wave front evolution between them. After all science and reference observations are complete, we perform the dedicated background observations that are used to subtract the dominant “glow stick” stray light feature (Boccaletti et al. 2022) as described in Section 2.1.

We begin data reduction using the Stage 0 (`*uncal.fits`) files as generated by the `jwst` pipeline. These products are then processed to Stage 1 (`*rateints.fits`) files using `spaceKLIP`. Similarly to NIRCcam (see Section 2.3), we explore the impact of the jump detection threshold on our analysis. For these data in particular, we found that the default jump detection threshold value of 4 is too low and leads to a number of pixels being erroneously flagged as containing a jump. Flagged pixels are interpreted differently from unflagged pixels in the ramp fitting procedure, and the resulting Stage 1 files contain a large number of pixels with unrealistic (negative) flux values as a result. After repeating an early version of our F1140C analysis across thresholds of 4–16, we observe an improvement in contrast between a threshold value of 4 and 5 of $\sim 2 \times 10^{-5}$ at $1''$, and $\sim 1 \times 10^{-5}$ at $2''$. Beyond this value, there is only slight improvement, and the obtained contrast varies by less than $\sim 5 \times 10^{-6}$ at $1''$. For our final analyses, we select a threshold value of 8, as it has the best contrast at $2''$ and fewer pixels with unrealistic flux values than lower thresholds (as determined from visual inspection).

Following ramp fitting, we found that the first integration of each exposure contained a significantly increased level of nonuniform noise, indicative of a detector reset charge decay anomaly, which is driven by differences in how the MIRI field effect transistors reset the detector charge prior to an exposure versus between integrations.⁷² Ideally, this anomaly can be corrected by calibration dark exposures; however, the currently available calibration darks were acquired in quick succession

⁷² <https://jwst-pipeline.readthedocs.io/en/latest/jwst/rscd/description.html>

and do not have an amount of dead time (e.g., due to telescope slews/dithers) similar to that of our science exposures. As a result, during our observations, the detector electronics were given a much longer time to settle, and our integrations exhibit an entirely different reset anomaly. This effect is most dominant for the first integration of each exposure, but appears to persist throughout the entire exposure as well. Quantitatively, the median flux of the first integration following background subtraction (see below) for the target/reference observations are $6.2/3.0\sigma$ and $7.3/3.9\sigma$ deviant from the average median flux across all integrations for the F1140C and F1550C observations, respectively. In comparison, the median flux of all other target/reference integrations deviates within ranges of $0.003-0.59/0.26-0.55\sigma$ and $0.004-1.29/0.06-0.86\sigma$ for the F1140C and F1550C observations, respectively. As this increased noise is not accurately captured in the available calibration files and differs significantly from all other integrations, we opt to exclude the first integration of each exposure from all further analysis. This exclusion corresponds to a 2.5%/10% and a 1.7%/5.3% cut of the target/reference data for the F1140C and F1550C observations, respectively. In the future, better dark exposures will be taken as part of observatory calibrations that may well remove the need to exclude the first integration, and we encourage future observers to carefully evaluate the calibration status of their data before adopting similar cuts.

The Stage 1 products are processed further to Stage 2 (*calints.fits) files using `spaceKLIP`, with some additional pixel cleaning procedures as follows. First, every pixel with a data quality flag (e.g., indicating hot pixels, warm pixels, or unreliable data processing) is replaced by the median of its orthogonal and diagonal neighbors, with the notable exclusion of pixels with a jump flag, which are typically grouped in clusters. Following this correction, ~ 30 static hot pixels remain in our images and are corrected following an identical procedure by manually providing the pixel locations to `spaceKLIP`. Similarly to NIRCcam, these final pixels primarily impact the measured contrast performance, and not our ability to recover HIP 65426b.

As shown in Boccaletti et al. (2022), the MIRI coronagraphic fields of view are subjected to a stray light “glow stick” feature along the horizontal edges of the FQPMs that dwarfs the residual stellar flux (see Figure 2). We subtract this feature from our processed Stage 2 products for each filter using a median background image of every 4–5 integrations from the dedicated background observations to the corresponding 4–5 science or reference integrations. The value of 4–5 was selected because it provided a slightly improved contrast at $1''$ compared to other tested numbers of integrations per median, ranging from 1 ($\sim 1 \times 10^{-4}$ improvement) to all available integrations ($\sim 1 \times 10^{-5}$ improvement). Grouping the median subtraction in this manner better captures the diffuse reset anomaly noise between integrations mentioned above. Additionally, it may help capture variations in the stray light feature, which varies with a standard deviation of $\sim 0.5\%$ (as identified by variations in the median pixel flux for pixels above 50% of the peak pixel flux across integrations).

Following the median background subtraction, we find that the residual stellar flux is easily recovered (see Figure 2). We also attempted to model the stray light glow stick as a principal component within both KLIP (Soummer et al. 2014) and LOCI (Lafrenière et al. 2007) based subtractions, but found that they

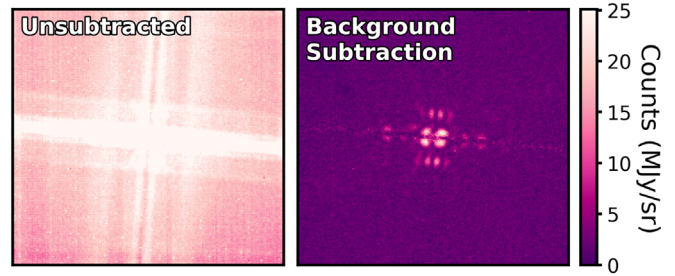


Figure 2. Left: A single integration in the Stage 2 (*calints.fits) file for MIRI coronagraphy of HIP 68245 in the F1550C filter. Right: As on the left, except following subtraction of a median background frame of an “empty” region of the sky. Both images are identically scaled. Before subtraction, the residual stellar flux is completely obscured by the stray light “glow stick” (Boccaletti et al. 2022), but it can be easily recovered.

were susceptible to oversubtraction of the residual stellar flux and/or could not additionally account for background variations between integrations. We anticipate that, with careful masking and optimization of these algorithms, it may be possible to overcome these issues; however, the median frame background subtraction is already highly effective and improvements to the achieved contrast are likely to be minimal.

2.5. Image Alignment

The NIRCcam and MIRI coronagraphic modes adopt independent target acquisition procedures to correctly center a star behind each focal plane mask. The in-flight positions of the NIRCcam mask centers are known to better than ~ 10 mas, but the distortion model is still being refined. At present, the target acquisition error for the MASK335R is as large as $\sim 12-30$ mas, or $0.2-0.5$ pixels (Girard et al. 2022). This error is dominated by the precision of the centering algorithm, which is not well adapted to the PSF shape with coronagraphic optics (wider in x -axis), and not by the small angle maneuver (SAM) that places a target at its desired position behind the mask (which for NIRCcam is repeatable to ~ 6 mas). For MIRI, the mask center positions have been measured to $\sim 5-10$ mas, or ~ 0.1 pixels (Boccaletti et al. 2022). However, the SAM has a typical uncertainty of $\sim 10-20$ mas, leading to positional offsets between different rolls or targets. Finally, between integrations, the pointing stability of JWST (~ 1 mas) and the accuracy of the small-grid dither maneuvers ($\sim 2-4$ mas) will lead to further positional shifts for both the NIRCcam and MIRI coronagraphs (Boccaletti et al. 2022; Rigby et al. 2023).

For NIRCcam, the absolute star position is only explicitly measured for the first science image in each filter. This position is measured using a cross correlation of a model coronagraphic PSF as obtained from `webbpsf_ext` to the science PSF using the `scikit-image` package (van der Walt et al. 2014). To best match the science PSF, the model PSF is generated using the telescope optical path difference (OPD) map as obtained on 2022 July 29th. To identify the accuracy of this process, we repeat the procedure, except comparing the model PSF to itself, and to a second model PSF that was generated using a prelaunch measurement of the telescope OPD (which exhibits comparable differences from the model PSF as our data). In each case, we manually shift the comparison PSFs across a range of $0.01-0.5$ pixels and attempt to recover these offsets using the cross-correlation process. For the self-comparison, we recover the injected shift to at least ~ 0.03 pixels, or 1.9 mas,

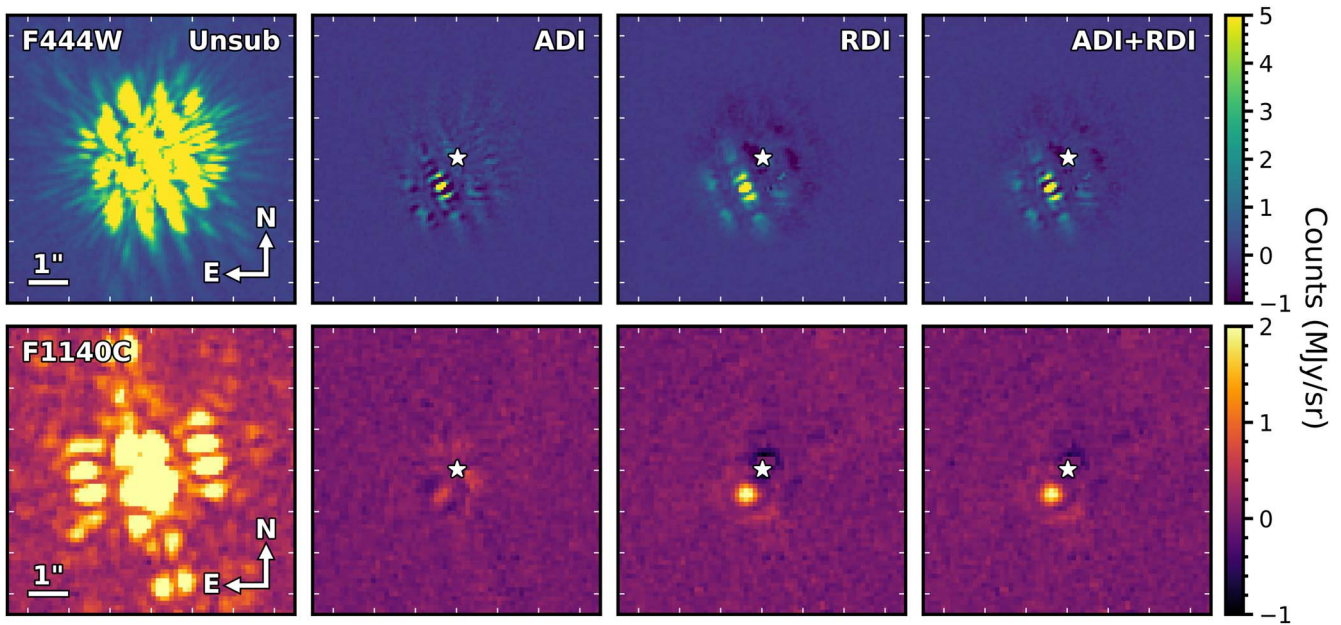


Figure 3. Unsubtracted and KLIP subtracted image stamps for the NIRCAM F444W (top row) and MIRI F1140C (bottom row) filters. The leftmost column displays the median unsubtracted image for a single science roll, and all other columns display the KLIP subtracted images for ADI, RDI, and ADI+RDI subtraction methods using the maximum number of KLIP PCA modes. All images are oriented as shown by the directional arrow in unsubtracted image column; the position of the star (white star) is also marked. Additionally, the intensity of all images for a given filter are identically scaled. The exoplanet, HIP 65426b, can be easily identified at a position angle of $\sim 150^\circ$ in the subtracted images. We note that the distinct “hamburger” shaped central core and six-lobed structure of the companion PSF in the NIRCAM images are expected features that are related to the Lyot stop design, and these are not indicative of discrete astrophysical sources.

whereas for the second model PSF comparison, we recover the injected shift to ~ 0.1 pixels, or 6.3 mas. Given the comparable difference between the model PSF for both the second model PSF and our data, we adopt the latter uncertainty as a systematic uncertainty in our astrometric measurements (see 5.1). The shifts of the other science and reference images are obtained relative to the first science image through a similar cross-correlation procedure. However, we instead use a box of 11×11 pixels around the coronagraph center position, where the flux is dominated by the central core of the coronagraphic PSF. All measured relative shifts match expectations for the JWST pointing precision of ~ 1 mas (1σ , radial) (Rigby et al. 2023).

To estimate the absolute star position for MIRI, we use the current measurements for the centers of the coronagraphic masks and assume the star is perfectly centered behind the coronagraphic mask. In zero-indexed subarray x - y coordinates these values are (119.749, 112.236) and (119.746, 113.289) for the FQPM1140 and FQPM1550, respectively (Jonathan Aguilar, private communication). As a result, the stellar position is not known better than a minimum of ~ 10 mas (Boccaletti et al. 2022). Similarly, the relative alignment between images may be discrepant by ~ 1 – 4 mas (Rigby et al. 2023), or < 0.05 pixels. Attempts to estimate the absolute star position in a similar manner to the NIRCAM data were unsuccessful, and this process led to significantly larger estimated shifts than the known pointing stability of JWST (~ 50 mas, versus ~ 1 mas). This is most likely due to the variable spatial structure of the residual PSF, which significantly changes with small pointing shifts. An effort was also made to fit each MIRI image with model PSFs across all feasible pointings using `webbpsf_ext`⁷³ within an `emcee` (Foreman-Mackey et al. 2013) Markov Chain Monte Carlo (MCMC) framework. However, these fits were unable to converge, and upon visual

inspection, the spatial structure of the empirical and model PSFs were different, despite modeling the PSFs based on measurements of the telescope OPD within ~ 1 day of our observations. We do not believe that using the coronagraphic mask centers as a proxy for the absolute star position has significantly affected our results, but it is certainly an area of improvement for future studies using MIRI coronagraphy.

For NIRCAM, all images are aligned to a common center based on the measured shifts; however, for MIRI, we opt to not perform any realignment. This decision is made under the assumption that, because a pointing shift does not primarily cause a translation of the residual PSF in the MIRI images (in contrast to NIRCAM), the unshifted reference images are more descriptive of variations in the science images. When comparing an RDI subtraction using unshifted reference images versus a separate RDI subtraction with a realignment based on the ideal small-grid dither positions, the measured contrasts are in agreement and this choice does not significantly impact our results.

2.6. PSF Subtraction

We perform a subtraction of the residual stellar PSF in each filter following three different principal component analysis (PCA) based methods as implemented in `spaceKLIP`. First, we take the two independent rolls of HIP 65426b and perform an ADI subtraction. Second, we perform an RDI subtraction by using the corresponding observations of the reference star, HIP 68245, as a PSF library. Finally, we perform an ADI+RDI subtraction, which is identical to the RDI subtraction except that images at the opposite roll angle are also included in the PSF library. In each case, the subtraction is performed on each integration from both science rolls individually, before being rotated to a common orientation as marked in Figure 3 and summed together. Although the number of annuli and subsections the PSF subtraction is performed across can be

⁷³ https://github.com/JarronL/webbpsf_ext

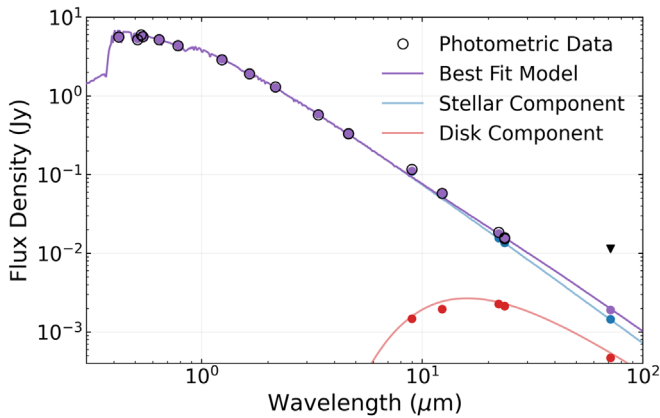


Figure 4. The best-fit stellar model (purple) to existing Hipparcos/Tycho-2, Gaia DR2, 2MASS, ALLWISE, AKARI IRC, and Spitzer MIPS data for HIP 65426 (black circles). The stellar (blue) and disk (red) components of the model are also shown, along with the equivalent model fluxes in each photometric band (solid circles). Error bars are smaller than the circle diameter, except for the 70 μm MIPS point, which is instead marked as an upper limit (black triangle).

adjusted, we find that this does not improve the observed contrast. Hence, we perform all subtractions using a single annulus and a single subsection (i.e., the entire image). We leave future optimization of these parameters for future analysis, but we note that any improvements to the measured contrast are likely to be small, as the noise in our images is close to azimuthally symmetric. The number of KLIP PCA modes can also be adjusted to tune the aggressiveness of the PSF subtraction. Hence, we perform the PSF subtraction across the full range of possible PCA modes, to investigate the impact on our measured contrast and companion fitting. The maximum number of PCA modes is dependent on the exposure settings for each filter and corresponds to the number of integrations in a single roll for ADI, the total number of integrations across all nine dithers for RDI, and the sum of the two for ADI+RDI (see Table 1 for precise values).

Pre- and post-subtraction images for the NIRCcam F444W and MIRI F1140C filters are shown in Figure 3, and images for all filters are shown in Appendix A. We note that the distinct “hamburger” shaped central core and six-lobed structure of the companion PSF in the NIRCcam images are expected features that are related to the Lyot stop design, and these are not indicative of discrete astrophysical sources.

3. Analysis

3.1. Contrast Calibration

All proceeding contrast measurements are determined relative to a synthetic spectrum of HIP 65426 in each of the JWST filters, as estimated from fitting stellar and disk models to existing photometry following Yelverton et al. (2019); see Figure 4. We use data of HIP 65426 from Hipparcos/Tycho-2 (Høg et al. 2000), Gaia DR2 (Gaia Collaboration 2018), 2MASS (Cutri et al. 2003), ALLWISE (Wright et al. 2010), AKARI IRC (Ishihara et al. 2010), and Spitzer MIPS (Chen et al. 2012). The fitting procedure compares synthetic photometry of models to the data to compute a χ^2 value, and posterior distributions are found using MultiNest (Feroz et al. 2009; Buchner et al. 2014). We derive our own zero points using the CALSPEC Vega spectrum (Bohlin et al. 2014). We use PHOENIX models (Allard et al. 2012) for the

stellar photosphere, and a Planck function for the disk model. There is a small excess at 24 μm that was previously reported at 3.5σ by Chen et al. (2012), though it was not considered significant in that paper. The best-fit model has an effective temperature of 8600 ± 200 K and luminosity $16 \pm 1 L_{\odot}$. The dust temperature and luminosity are very poorly constrained ($T_{\text{dust}} = 300^{+200}_{-100}$ K, and $L_{\text{dust}}/L_{\star} \sim 2 \times 10^{-5}$), though this uncertainty does not significantly impact the flux estimation in JWST bandpasses, because the excess is small. The flux excess at 24 μm is not high, but if real, the dust would reside relatively close to the star, probably less than 1 au (hence we use the total model flux to compute the contrast, as any dust component that contributes IR flux would remain unresolved). We use the posterior distribution of model parameters and synthetic photometry to generate a distribution of fluxes in the JWST bands, and we adopt the maximum likelihood solution for the stellar flux in each bandpass.

3.2. Contrast Curves

Following PSF subtraction, we obtain metrics of the sensitivity as a function of angular separation (i.e., contrast curves) for all observational filters using spaceKLIP. To avoid biasing the contrast measurement we mask regions of the subtracted images near HIP 65426b, background sources, and the FQPM edges. These “ 5σ ” contrast curves report the flux level corresponding to a 5σ -equivalent false-alarm probability of 2.9×10^{-7} after correcting for small sample statistics at small separations (Mawet et al. 2014). We call them 5σ contrast curves, for brevity.

To obtain a more accurate measurement of the contrast performance, the throughput of the coronagraph and the intrinsic throughput of the KLIP subtraction must be accounted for by injecting and then recovering the flux of artificial sources (Adams & Wang 2020). All artificial sources are generated using `webbpsf`⁷⁴ (Perrin et al. 2012, 2014) at an initial intensity equivalent to a signal-to-noise ratio of 25. Immediately prior to injection and based on a desired injection location, each source is modulated by the coronagraphic throughput using a synthetic throughput map.

Synthetic coronagraphic throughput maps are provided in the calibration reference files;⁷⁵ however, both the provided NIRCcam and MIRI FQPM maps are inaccurate. For the NIRCcam MASK335R, the position of the occulting mask within the throughput map does not correspond with its actual location. Therefore, we modify the throughput map by extracting the pixels impacted by the occulting mask and repositioning them at the true mask center location of (149.9, 174.4) in zero-indexed subarray x - y coordinates (Jarron Leisenring, private communication). In the case of MIRI, all of the FQPM maps are rudimentary and do not accurately capture the spatial throughput variations. Therefore, we instead use custom simulated maps of the FQPM throughput produced using `Webbpsf`. In brief, for each coronagraphic mode, we generate 1681 position-dependent PSFs across a $25'' \times 6$ by $25'' \times 6$ grid spanning the subarray field of view (FOV). The PSFs are generated with logarithmic spacing such that they are most densely sampled along the FQPM axes. For each position in the FOV, we calculate two PSFs, one occulted and one unocculted, and take the ratio of the integrated PSF fluxes in each case to

⁷⁴ <https://webbpsf.readthedocs.io/en/latest/>

⁷⁵ <https://jwst-crds.stsci.edu>

Table 2
Filter-dependent PSF Offsets Relative to the Center of the NIRCcam MASK335R as Defined by the F335M Filter

Filter	dx (pixels)	dy (pixels)
F250M	0.086 ± 0.014	-2.049 ± 0.012
F300M	0.078 ± 0.014	-0.531 ± 0.016
F356W	0.751 ± 0.010	-0.121 ± 0.009
F410M	0.177 ± 0.013	-0.086 ± 0.021
F444W	0.157 ± 0.015	-0.224 ± 0.039

provide a throughput estimate at each position. From this 2D sampling of throughput, we use `scipy.interpolate.griddata` to linearly interpolate the throughput estimates across the FOV to produce a smooth 2D map matching the subarray dimensions for each MIRI FQPM.

Due to the target acquisition errors described in Section 2.5, the measured star centers are offset from the center of the coronagraphic occulter. However, in addition to these pointing errors, for NIRCcam coronagraphy we expect wavelength-dependent spatial shifts of the entire image as viewed on the detector focal plane, due to refraction through the coronagraphic mask sapphire substrate along with deflections through filter optics further downstream in the optical train. Therefore, the star position in an image is not in isolation a suitable proxy for its position behind the coronagraphic mask. The wavelength-dependent shifts must be accounted for in order to more accurately determine the impact of the coronagraphic throughput across the detector focal plane and apply the correct throughput scaling to injected PSFs.

The aforementioned location for the MASK335R occulter at the detector focal plane is set based on the F335M filter, which is used for target acquisition and astrometric confirmation observations, and its image shift is defined to be zero. To measure the relative shifts of the remaining observational filters, we first determine the center of the projected stellar image for each filter observation of the science target roll positions and the reference target by cross-correlating an observed image in the Stage 1 `*rate.fits` file with a perfectly centered synthetic PSF generated with `webbpsf`. These synthetic PSFs are created using the on-sky OPD map from 2022 July 29, and are recentered to remove preflight model shifts, which do not fully capture contributions from all optical elements, such as the different filter optics. The measured subpixel locations for each observed filter are then compared to the similarly measured F335M astrometric confirmation image to determine the filter-dependent offsets. The two independent target rolls and reference exposures provide three independent measures that are averaged together and presented in Table 2; uncertainties are on the order of 1–2 mas. Finally, to apply the correct coronagraphic throughput to an injected synthetic planet in a given filter at a given position, we simply realign the throughput map according to the measured offset for that filter.

Once scaled by the coronagraphic throughput, PSFs are injected into multiple copies of the unsubtracted science images across a range of separations extending to $4''$, and for a range of position angles from 0° to 360° . Sources are not injected within $2\lambda/D$ of each other or a masked region. These images then undergo KLIP subtraction in an identical manner to the science images, and the relative flux of an initial source PSF and the KLIP processed PSF as estimated within `pyKLIP` describes

the overall coronagraphic mask plus KLIP throughput at each location. Finally, the basic 5σ contrast is divided by an interpolation of the median throughput across all position angles, to obtain the calibrated contrast.

For the ADI subtraction, the measured contrast does not vary significantly when using more than one PCA mode for the NIRCcam filters and more than two PCA modes for the MIRI filters. For RDI, the measured contrast does not vary beyond ~ 6 modes for both NIRCcam and MIRI. Finally, for ADI+RDI, we find that there is a transition to improved contrast at $P_{\max} - P_{\text{ADI}}$ modes, where P_{\max} is the maximum possible number of PCA modes possible, and P_{ADI} is the maximum number of modes for the ADI subtraction. This is likely a result of the much larger number of reference images weighting the calculation of the PCA modes to be mostly RDI-like, until a sufficient limit is reached where the influence of the opposing roll images appears in the principal components. Beyond this transition value, the measured contrast does not vary significantly.

Example calibrated contrast curves for the NIRCcam F444W and MIRI F1140C filters using the maximum number of PCA modes are shown in Figure 5, and contrast curves for all filters are shown in Appendix B.

3.3. HIP 65426b PSF Fitting

To analyze the properties of HIP 65426b in greater detail, we make use of the forward model PSF fitting routine provided by `pyKLIP` and implemented in `spaceKLIP`. Briefly, this routine takes a model of the companion PSF and uses a forward model of the KLIP subtraction to apply PSF distortions that arise naturally from the KLIP process. This resultant PSF can then be scaled/shifted to best match the observed companion PSF and obtain a measurement of its location and intensity (Pueyo 2016; Wang et al. 2016).

For our analysis, we adopt an independent model PSF for each filter using `webbpsf_ext` functionality as implemented in `spaceKLIP`. Specifically, we use `webbpsf_ext` to generate an offset PSF at the predicted location of HIP 65426b as adopted from `whereistheplanet` (Wang et al. 2021) and at the appropriate position for each science roll image. Each NIRCcam and MIRI PSF is generated using a measured OPD map as determined from wave front sensing and control observations on 2022 July 29th and 2022 July 17th, respectively. In particular for MIRI, the PSF of an off-axis source is still sensitive to its location relative to the FQPM edges, and explicitly generating a model PSF close to this location is important for obtaining a close match to the true companion PSF. As the spatial intensity of the model PSF depends on an assumed spectral energy distribution (SED), we use an existing best-fit BT-SETTL model for HIP 65426b from Cheetham et al. (2019). We note that, as the initial model PSF is normalized to unit intensity, the primary purpose of selecting a model SED is not to accurately predict the absolute flux of HIP 65426b in each bandpass, but instead to capture the relative variation in flux as a function of wavelength across each bandpass (which is largest for the broader NIRCcam wide filters). Finally, the impact of the coronagraphic throughput on the received flux is applied by multiplying the normalized PSF by a scale factor equal to the relative difference between the integrated flux of the model PSF prior to normalization and a matching `webbpsf_ext` model PSF that excludes the coronagraphic elements.

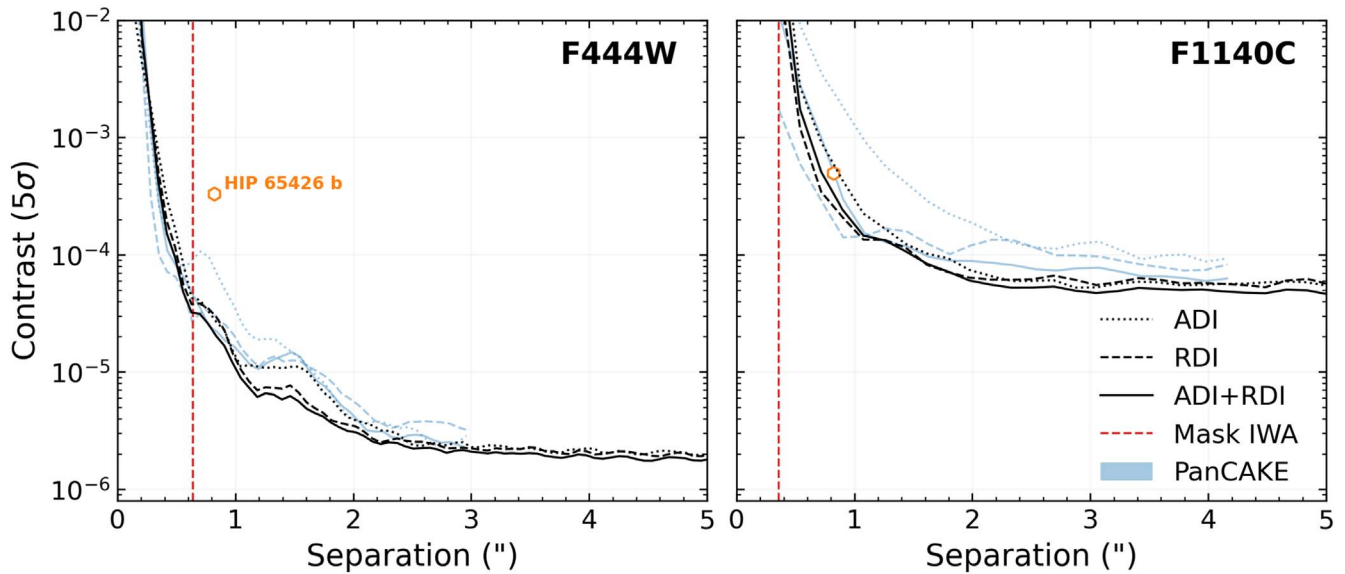


Figure 5. Contrast curves for observations in the F444W and F1140C filters using an ADI (dotted lines), an RDI (dashed lines), and an ADI+RDI (solid lines) subtraction using 20 PCA modes. Both the measured contrast of the true on-sky observations (black lines) and predicted contrasts as generated from PanCAKE (Carter et al. 2021b) (light blue lines) are displayed. The effective inner working angles (IWA) corresponding to the separation at 50% transmission (red dashed lines), and the companion HIP 65426b (orange hexagon), are also marked. Contrast curves for all other filters are displayed in Figure 14.

The input model PSF is converted to physical units by scaling it to the flux of HIP 65426 as estimated by the stellar model described in Section 3.1. Therefore, all derived photometry is anchored relative to our assumption of the stellar flux. Furthermore, any comparisons between the intensity of this PSF and the observed PSF are subject to an implicit assumption that the absolute flux calibration of JWST is perfect. In reality, the absolute flux calibration accuracy requirements for NIRCcam and MIRI coronagraphy are 5% and 15%, respectively.⁷⁶ Both these fundamental uncertainties on the absolute flux calibration and the uncertainty on the stellar model flux as derived from the distributions described in Section 3.1 are propagated as an increased uncertainty on all of our flux measurements.

For each filter, we fit the location and intensity of the model PSF to the true PSF of HIP 65426b from the ADI+RDI subtraction using six PCA modes. The fitting procedure is executed in an MCMC framework as implemented by `emcee` (Foreman-Mackey et al. 2013), with 50 walkers for 2200 steps, of which the first 200 steps are discarded as burn-in. `spaceKLIP` allows for the spatial scale of noise in an image to be fit with a variety of different kernels as implemented in a Gaussian process framework. For NIRCcam, the noise in our images appears to be correlated at the separation of HIP 65426b, so, following Wang et al. (2016), we initially adopt a Matérn 3/2 kernel to better capture this spatially correlated noise structure. However, the generated model PSF is slightly mismatched to the observed data, and a positive flux residual was present at the PSF core. Future improvements to model PSF generation may alleviate this issue, but in this work we instead assume uncorrelated noise (using the “diagonal kernel” option), which is able to better capture the flux of the companion at the expense of underestimating the obtained error bars. Therefore, more realistic error bars for the NIRCcam photometric measurements are determined through a process of companion injection and recovery. For each filter, the best-fit

model PSF is used to subtract away the companion flux and is then injected at 20 different position angles spanning 0° – 105° and 195° – 360° across an equivalent number of duplicate science images. The HIP 65426b PSF fitting procedure is then repeated on these synthetic PSFs, and the standard deviation in the measured flux across all 20 position angles is adopted as the estimated error. In the case of MIRI, the observed noise is visually consistent with uncorrelated noise, so we adopt a diagonal kernel here as well.

Results from the PSF fitting procedure are discussed further in Section 5, and images of the data, model, and residuals to each PSF fit are displayed in Appendix C.

4. Instrument Performance

4.1. Achieved Contrast

These observations provide a first look at the achieved contrast for JWST’s high-contrast imaging modes following the completion of observatory commissioning, and they demonstrate that, in addition to the existing work of Girard et al. (2022), Kammerer et al. (2022), and Boccaletti et al. (2022), both NIRCcam and MIRI coronagraphic imaging are exceeding their predicted contrast performance. Examples of this improvement in comparison to prelaunch contrast estimates as obtained by PanCAKE (Carter et al. 2021b) are demonstrated in Figure 5, and contrast curves for all seven filters are displayed in Appendix B.

At the MASK335R nominal IWA of $0''.63$, the F444W data achieve a contrast of $\sim 4 \times 10^{-5}$, sloping down to $\sim 1 \times 10^{-5}$ at $1''$ and then $\sim 2 \times 10^{-6}$ beyond $3''$. In comparison, at the FQPM1140C nominal IWA of $0''.36$, the MIRI F1140C data achieve a contrast $\sim 1 \times 10^{-2}$, sloping down to $\sim 2 \times 10^{-4}$ at $1''$ and then $\sim 5 \times 10^{-5}$ beyond $3''$. For brevity, we do not describe the achieved contrast in the other filters, and instead we refer the reader to Appendix B.

In the background-limited regime beyond $2''$, the measured contrasts for NIRCcam approximately match the predicted sensitivity of the ADI and ADI+RDI subtractions, and they are

⁷⁶ <https://jwst-docs.stsci.edu/jwst-data-calibration-considerations>

up to two times more sensitive than the prediction for the RDI subtraction. For MIRI in this regime, all three subtraction methods outperform their predicted sensitivity by a factor of 1.5–2. In the contrast-limited regime below $\sim 2''$, we observe further improvements upon the predicted contrast, with the ADI and RDI subtractions demonstrating a factor of up to 5–10 times deeper contrast, and the ADI+RDI subtraction improving by a factor of ~ 2 . In some instances, at the shortest separations below $\sim 0''.6$, the contrast does underperform by up to a factor of ~ 2 compared to predictions for RDI subtractions. The primary driver for these improvements is likely the improvement in the overall optical and stability performance of JWST compared to expectations. The total throughput is $\sim 10\%$ – 20% larger than predictions, driving analogous improvements in signal-to-noise; the overall telescope wave front error is $\sim 50\%$ smaller than requirements (75/110 nm versus 150/200 nm for NIRCам/MIRI), improving the raw contrast; and the pointing stability of 1 mas is ~ 6 – 7 times smaller than predictions, meaning smaller drifts in alignment behind the coronagraphic mask throughout an observation (Rigby et al. 2023).

The different contrasts as achieved by the ADI, RDI, and ADI+RDI subtractions allow for more concrete recommendations in observing structure for future programs. Most significantly, the improvement between RDI and ADI+RDI subtractions is negligible. Future observers will may be able to achieve their science goals with less telescope time by focusing on purely ADI or RDI subtraction strategies; however, a broader range of observations will be required in order to rule out ADI+RDI strategies entirely. Within $1''$ – $2''$, the ADI subtraction for MIRI F1550C, and to some extent F1140C, struggles to fully subtract the residual stellar PSF, and an RDI-based subtraction strategy should be preferred. Although RDI subtractions can provide improvements of up to 5–10 times deeper contrast below $1''$ for some filters (see Appendix B), this technique requires a larger amount of observing time due to the cost-intensive nature of dithered reference observations. These time costs can be reduced by performing a smaller number of reference dithers; however, this will in turn reduce the achieved contrast. For example, by comparing subtractions using individual reference dithers from a nine-point dither strategy, Girard et al. (2022) demonstrate a range of 2–10 times worse contrast at $1''$ compared to a subtraction combining all dithers in a PCA framework similar to that adopted for this work. A precise assessment of the trade space between contrast, observing time, dither pattern, and subtraction strategy for JWST coronagraphy is beyond the scope of this work. Nevertheless, future observers should use simulation tools such as PanCAKE (Carter et al. 2021b) to identify the contrast performance necessary to meet their science goals, and adjust their PSF subtraction strategy accordingly to improve observational efficiency.

Similar NIRCам and MIRI observations have been performed as part of observatory commissioning, and these are detailed in Girard et al. (2022), Kammerer et al. (2022), and Boccaletti et al. (2022). The observed contrast between this work and these commissioning efforts are in broad agreement, with the regime within $\sim 2''$ being contrast limited, and the regime beyond $\sim 2''$ being background limited. For the NIRCам F356W observation of HIP 65426 (0.5 Jy) in the background-limited regime, we reach sensitivities of $\sim 0.4 \mu\text{Jy}$ (~ 20 minute exposure time), compared to $\sim 1 \mu\text{Jy}$ in Kammerer et al. (2022) for HD 114174 (G3IV, 2MASS $K_s = 5.202$) in the F335M filter (2.6 Jy, ~ 55 minute exposure). For MIRI F1140C/F1150C observations of

HIP 65426 (0.06/0.03 Jy) in the background-limited regime, we reach sensitivities of $\sim 2.7/3 \mu\text{Jy}$ ($\sim 30/120$ minute exposure time), compared to $\sim 9/30 \mu\text{Jy}$ in Boccaletti et al. (2022) for HD 158165(K5V, 2MASS $K_s = 4.704$)/HD 163113(K0V, 2MASS $K_s = 2.749$) in the F1140C/F1150C filters (0.45/1.45 Jy, $\sim 75/150$ minute exposure time). Differences in these measured sensitivities are likely driven by the complex interplay of source spectral type, magnitude, and exposure time, and will be better understood in the context of a broader range of future JWST coronagraphic observations.

Beyond this work, there is significant potential for the contrast performance for both NIRCам and MIRI to improve. Kammerer et al. (2022) have already demonstrated that the NIRCам bar masks can provide deeper contrasts at shorter separations, if a full 360° field of view is not required. Similarly, in later cycles, it may be possible to position a star at the “NARROW” bar mask position in an attempt to reduce the effective inner working angle (IWA) even further. The efficacy of RDI subtractions may improve with the use of a larger PSF library populated by on-sky observations across multiple programs. It may also be possible to perform an effective PSF subtraction using a much larger PSF library composed either entirely or partially of model PSFs. A particular opportunity for improvement will also come from JWST program GO-02627 (Ygouf et al. 2021), which aims to estimate the on-sky instrumental aberrations that drive variations in the observed PSF structure with a model-based phase retrieval algorithm.

4.2. Mass Sensitivity

Using the obtained contrast curves, we also determine the detectable mass limits for our observations following the approach of Carter et al. (2021a). Briefly, we convert our contrast curves to magnitude sensitivity curves using the stellar magnitudes as described in Section 3.1, and then convert these to a mass sensitivity using an interpolation of the evolutionary models of Linder et al. (2019) (BEX) and Phillips et al. (2020) (ATMO) assuming an age of 14 ± 4 Myr (Chauvin et al. 2017) and distance of 107.49 ± 0.40 pc (Gaia Collaboration 2021). As in Carter et al. (2021a), we select the chemical equilibrium, noncloudy models to maintain model consistency across mass ranges. Clouds and disequilibrium chemistry likely play a significant role in sculpting the emission of substellar atmospheres; however, an investigation into these effects is beyond the scope of this work.

Following the calculation of mass sensitivity curves, we use the Exoplanet Detection Map Calculator (Exo-DMC; Bonavita et al. 2012, 2013; Bonavita 2020)⁷⁷ to estimate detection probability maps. In this case, we produce a population of synthetic companions with masses and semimajor axes from $0.1 M_{\text{Jup}}$ to $100 M_{\text{Jup}}$ and 0.1 au to 10,000 au, respectively. The inclination is uniformly distributed in $\sin(i)$, the eccentricity is distributed using a Gaussian with $\mu = 0$ and $\sigma = 0.3$ (excluding negative eccentricities; Hogg et al. 2010), and all other orbital parameters are uniformly distributed. Implicit in this is an assumption that these synthetic companions do not necessarily have a similar inclination to HIP 65426b. The resulting map takes into account the effects of projection when estimating the detection probability, as well as the probability for a potential companion to truly lie in the instrumental field of view.

⁷⁷ https://github.com/mbonav/Exo_DMC

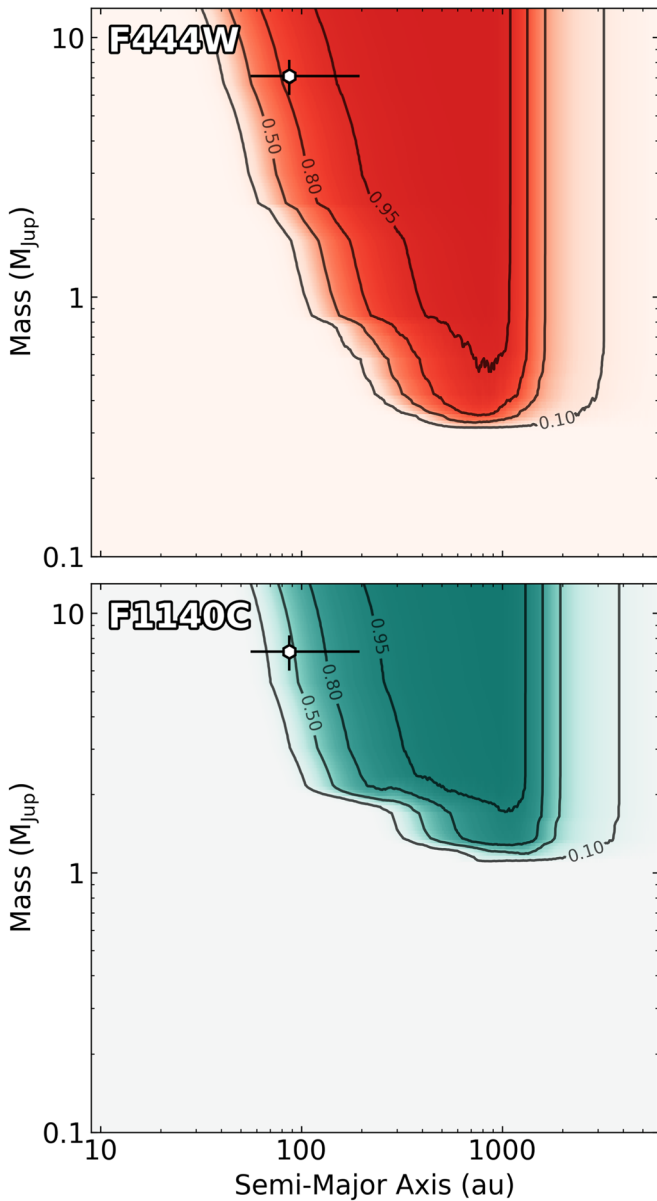


Figure 6. Detection probability maps as generated by `EXO-DMC` for the most sensitive NIRCcam (F444W, top) and MIRI (F1140C, bottom) filters. Solid black contours signify the 10%, 50%, 80%, and 95% detection thresholds. The true location of HIP 65426b is marked (hexagon) with errors taken from the astrometric fitting in Section 5.1, and evolutionary model analysis in Section 5.4.

For these particular observations of HIP 65426, we identify the F444W and F1140C filters as the most sensitive to the lowest-mass companions for NIRCcam and MIRI, respectively, and display their detection probability maps in Figure 6. Of the two, the F444W filter is the most sensitive, reaching a sub-Jupiter-mass sensitivity from ~ 150 to 2000 au at a 50% probability, and a minimum sensitivity of $\sim 0.4 M_{\text{Jup}}$ (~ 350 K) ~ 300 –1500 au at a 50% probability. In contrast, the F1140C is unable to reach sub-Jupiter-mass sensitivity, and it has a minimum sensitivity of $1.5 M_{\text{Jup}}$ (~ 550 K) from ~ 150 to 2000 au. As we detect no sources within the observed field of view that have colors consistent with a planetary-mass companion, we set equivalent limits on the presence of additional companions in the HIP 65426 system.

Despite the F444W observation being at a shorter wavelength, corresponding to a finer angular resolution, it does not probe significantly closer separations than the F1140C observation. This is driven by the competing influence of the larger IWA for the NIRCcam MASK335R of $\sim 0''.63$, compared to $\sim 0''.36$ for the MIRI FQPM1140C (both assumed at 50% transmission radius). At the wider separations, the F444W observation is sensitive to the lower-mass companions than the F1140C observation, due to the lower thermal background, which is ~ 100 times fainter at $4.5 \mu\text{m}$ compared to $11.3 \mu\text{m}$ (Rigby et al. 2023).⁷⁸

As discussed in Carter et al. (2021a), at a given distance, A stars are generally poor targets for detecting the lowest-mass planets in terms of detection sensitivity, whereas M stars are among the most favorable. Given the improved performance of JWST, it is likely that, for nearby targets within (or outside of) the M-star sample from Carter et al. (2021a), it will be possible to detect Uranus- and Neptune-mass objects beyond ~ 100 –200 au, and Saturn-mass objects beyond ~ 10 au. Initial searches across a small sample of stars for sub-Jupiter-mass objects will be performed as part of guaranteed time observations (Schlieder et al. 2017). Furthermore, for the nearest targets, we may be able to push these limits even further, with planned observations of α Cen A aiming to be sensitive to $5 R_{\oplus}$ companions from 0.5 to 2.5 au (Beichman et al. 2020, 2021).

5. HIP 65426b in Context

The known companion HIP 65426b is clearly detected in all seven of the observational filters using RDI, and in all filters except the MIRI F1550C using ADI. These observations represent the first images of an exoplanet to be obtained with JWST, and the first-ever direct detection of an exoplanet beyond $5 \mu\text{m}$.

5.1. Astrometry

The measured astrometry in each of the observed filters is obtained from the ADI+RDI reduction and shown in Table 3. Each of the measured uncertainties for the NIRCcam astrometry are propagated with an additional uncertainty of 6.3 mas (0.1 pixels), and the uncertainties of the MIRI astrometry are propagated with an additional uncertainty of 10 mas (0.1 pixels) to account for the assumed precision of the absolute star centering as described in 2.5. All NIRCcam and MIRI astrometry are consistent within 1σ , and in combination the NIRCcam and MIRI astrometry provide a measurement of the separation, $\rho = 819 \pm 6$ mas, and the position angle, $\theta = 149^{\circ}8 \pm 0^{\circ}4$. To compute these average values, we do not treat the NIRCcam filters as independent, and instead we average both the quantities and their uncertainties. The absolute position of the star on the detector does not change significantly (< 1 pixel) between NIRCcam filters, and it is feasible that the measured position has a similar systematic offset in each filter (see Section 2.5). As the dominant noise source for the NIRCcam alignment is this systematic offset, it is not appropriate to propagate the uncertainties of the NIRCcam astrometry in a typical fashion.

We combine these new measurements with the existing astrometry from Chauvin et al. (2017) and Cheetham et al.

⁷⁸ <https://jwst-docs.stsci.edu/jwst-general-support/jwst-background-model>

Table 3
JWST Astrometry and Photometry of HIP 65426b

Filter	ρ (mas)	θ (deg)	m_* (mag)	Δ (mag)	Δ_{corr} (mag)	m_b (mag)	Flux ($\text{Wm}^{-2}\mu\text{m}^{-1}$)
F250M	822 ± 7	149.7 ± 0.5	6.783 ± 0.054	10.132 ± 0.032	10.132 ± 0.057	16.915 ± 0.083	$(4.29 \pm 0.33) \times 10^{-17}$
F300M	821 ± 6	149.8 ± 0.4	6.766 ± 0.046	9.829 ± 0.027	9.829 ± 0.056	16.595 ± 0.076	$(2.89 \pm 0.20) \times 10^{-17}$
F356W	816 ± 6	150.0 ± 0.4	6.767 ± 0.048	8.980 ± 0.015	8.980 ± 0.055	15.747 ± 0.074	$(3.36 \pm 0.23) \times 10^{-17}$
F410M	816 ± 6	149.8 ± 0.4	6.765 ± 0.051	8.734 ± 0.019	8.734 ± 0.055	15.499 ± 0.077	$(2.49 \pm 0.18) \times 10^{-17}$
F444W	820 ± 6	149.9 ± 0.4	6.764 ± 0.054	8.703 ± 0.015	8.703 ± 0.055	15.467 ± 0.078	$(1.97 \pm 0.13) \times 10^{-17}$
F1140C	823 ± 11	149 ± 1	6.722 ± 0.038	8.264 ± 0.021	8.264 ± 0.164	14.986 ± 0.169	$(7.40 \pm 1.16) \times 10^{-19}$
F1550C	836 ± 15	149 ± 1	6.766 ± 0.072	8.029 ± 0.039	8.029 ± 0.167	14.705 ± 0.182	$(2.74 \pm 0.46) \times 10^{-19}$

Note. m_* corresponds to the stellar magnitude in each filter, and Δ_{corr} corresponds to the relative magnitude following the propagation in uncertainties of a 5% or 15% absolute flux calibration accuracy for NIRCcam and MIRI, respectively. The position angle (θ) is provided from north through east, and all apparent magnitudes are relative to Vega.

(2019) to determine updated orbital parameters using the `orbitize!` package (Blunt et al. 2020). As in Cheetham et al. (2019), we exclude the NaCo epochs due to the inconsistency with the SPHERE epochs. Additionally, we exclude the MIRI epoch, because the observations were taken just two weeks after the NIRCcam observations and have larger uncertainties. `orbitize!` is initialized assuming one companion to the primary (HIP 65426b), a total system mass of $1.97 \pm 0.046 M_{\odot}$ (Chauvin et al. 2004), and a parallax of 9.3031 ± 0.0346 mas (Gaia Collaboration 2021). Orbit generation is performed using the Orbits for the Impatient (OFTI) algorithm (Blunt et al. 2020) until 100,000 possible orbits are identified. A random sample of 100 of the possible orbits along with posterior distributions for the entire sample are shown in Figure 7. We are able to constrain the semimajor axis, $a = 86_{-31}^{+116}$ au, and the inclination, $i = 99_{-6}^{+14}$ degrees (relative to the equatorial plane). Additionally, as the motion of HIP 65426b is primarily radial, solutions that place the line of nodes close to its position angle are preferred, and the position angle of nodes is also constrained to two possible solutions.

The addition of the NIRCcam astrometry does not significantly improve the orbital constraints for HIP 65426b, and all retrieved properties are consistent with those from Cheetham et al. (2019) and Bowler et al. (2020). Although our eccentricity distribution more strongly favors higher eccentricities compared to Cheetham et al. (2019), it remains essentially unconstrained and should not be interpreted as evidence for a highly eccentric orbit for HIP 65426b. However, if this high eccentricity is real, it would give credence to the scenario proposed in Marleau et al. (2019), where HIP 65426b initially formed through core accretion before being scattered to a wider separation by an additional companion. The ability of JWST to provide high-precision astrometry may improve with improvements to the measurement of the absolute star position in the NIRCcam images, which in this case is limited by the precision with which we can locate the star center behind the coronagraphic mask (see Section 2.5).

Separately from JWST, HIP 65426b has been observed using VLT interferometry as part of the ExoGRAVITY program (Lacour et al. 2020, Program ID: 1104.C-0651), which has routinely demonstrated submilliarcseconds astrometric precision (e.g., Gravity Collaboration et al. 2019; Lacour et al. 2021; Hinkley et al. 2023) and has an even greater potential to improve upon our reported constraints.

5.2. Photometry

As with the astrometry, the measured photometry in all of the observed filters is obtained from the ADI+RDI reduction and shown in Table 3, the subtracted images of all of these filters are shown in Figure 8, and the photometric data points themselves are shown in Figure 9. The measured contrast of the planet relative to the star ranges from 10.132 mag in the F250M filter to 8.029 mag in the F1550C filter. Images for the ADI and RDI subtractions can be found in Appendix A. Additional literature photometric measurements as shown in Figure 9 are provided in Appendix D.

5.3. Bolometric Luminosity

With the addition of JWST NIRCcam and MIRI photometric observations, the SED of HIP 65426b is measured across $1 \mu\text{m}$ to $15 \mu\text{m}$. The measurements span the majority of its luminous wavelength range and enable a tight constraint on the bolometric luminosity of the planet.

To calculate the luminosity, a full SED was created by distributing the flux density from photometric measurements over the effective bandwidth for each filter and using a model atmosphere to extrapolate beyond and interpolate between measured bands. Luminosity is then determined by integrating this semi-empirical SED over wavelength.

Because all of the flux measured in the NIRCcam/F410M photometry is accounted for in the F444W measurement, we used only the wider band for our analysis. We also added measurements from the literature at shorter wavelengths, including the SPHERE-IFS YH-band spectrum (Cheetham et al. 2019), and SPHERE-IRDIS H3, K1, and K2-band photometry (Chauvin et al. 2017; Cheetham et al. 2019; also see Appendix D).

To explore the dependence on the details of atmospheric model assumptions, we calculated the bolometric luminosity multiple times, using a broad range of models for interpolation and extrapolation of the SED. Atmospheric models spanned T_{eff} from 1200 to 1900 K and $\log(g)$ spanning 3.5–5.5. These models were drawn from three different grids, including two with different cloud implementations—BT-SETTL (Baraffe et al. 2015), and DRIFT-Phoenix (Witte et al. 2009)—and the cloud-free Sonora-Bobcat models (Marley et al. 2021). No matter which model we used to fill in the gaps between the measured portions of the SED, $\log(L_{\text{bol}}/L_{\odot})$ is always between -4.14 and -4.31 . Consequently, the luminosity is constrained at the 0.17 dex level and the result is robust across all considered model atmospheres. In totality, the measured

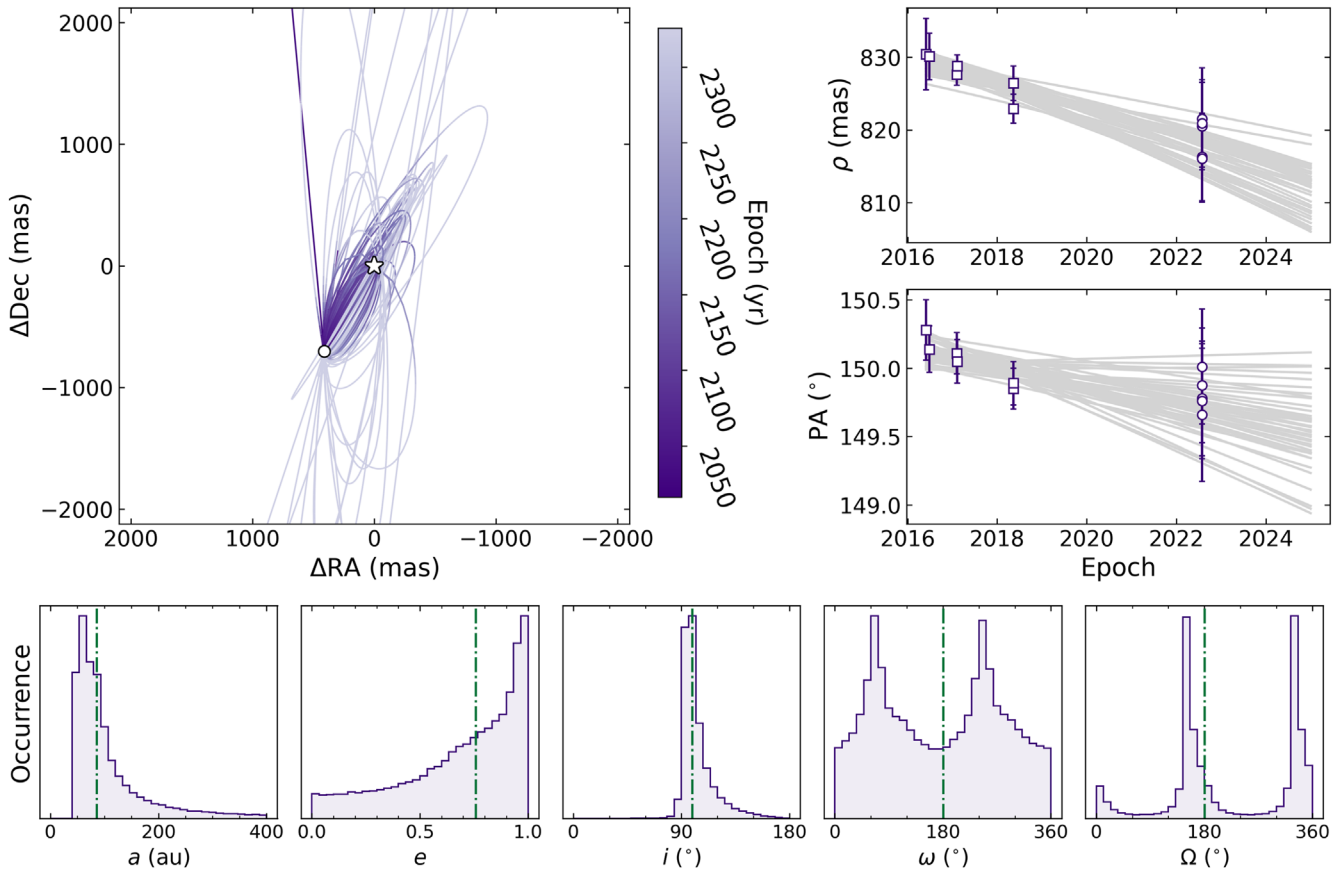


Figure 7. Orbital fitting of both JWST NIRCcam (this work) and SPHERE (Chauvin et al. 2017; Cheetham et al. 2019) astrometric measurements of HIP 65426b using *orbitize!* (Blunt et al. 2017). Top Left: A random sample of 100 orbit models from the retrieved posterior (purple curves). The positions of the planet (white circle) and the star (white star) are marked, and the epoch at a given position in an orbit is indicated by the color bar. Top Right: Separation and position angle vs. epoch for both the SPHERE (squares) and JWST NIRCcam astrometry (circles). The same random sample of 100 orbits is also displayed (gray lines). Bottom: Posterior distributions for the semimajor axis (a), eccentricity (e), inclination (i), argument of periastron (ω), and position angle of nodes (Ω). The 50% quantile from these distributions (green dotted-dashed line) are also indicated. In this particular case, these additional JWST observations do not significantly increase the constraints on the measured orbital parameters.

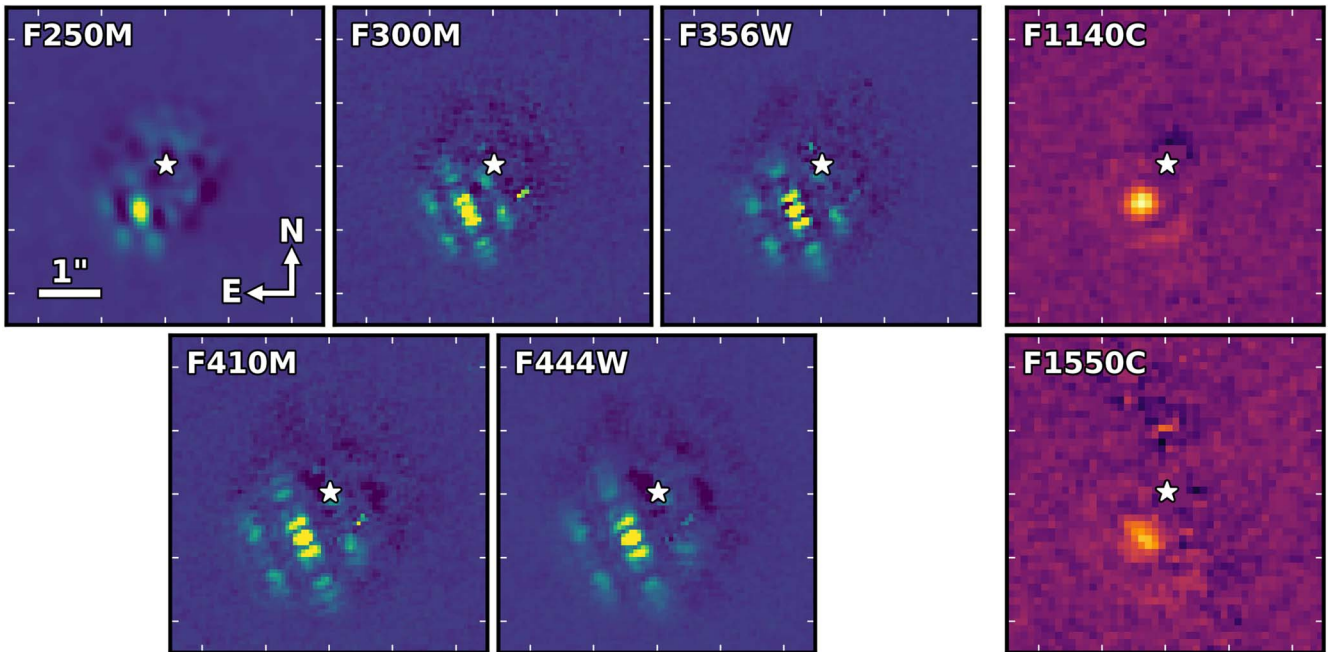


Figure 8. Images of the exoplanetary companion, HIP 65426b, in all seven NIRCcam and MIRI filters used in our observations. Each image is produced following an ADI+RDI KLIP subtraction of the residual stellar PSF. The measured position of the star is marked (white stars), and the orientation and pixel scales of all images are marked in the top left panel.

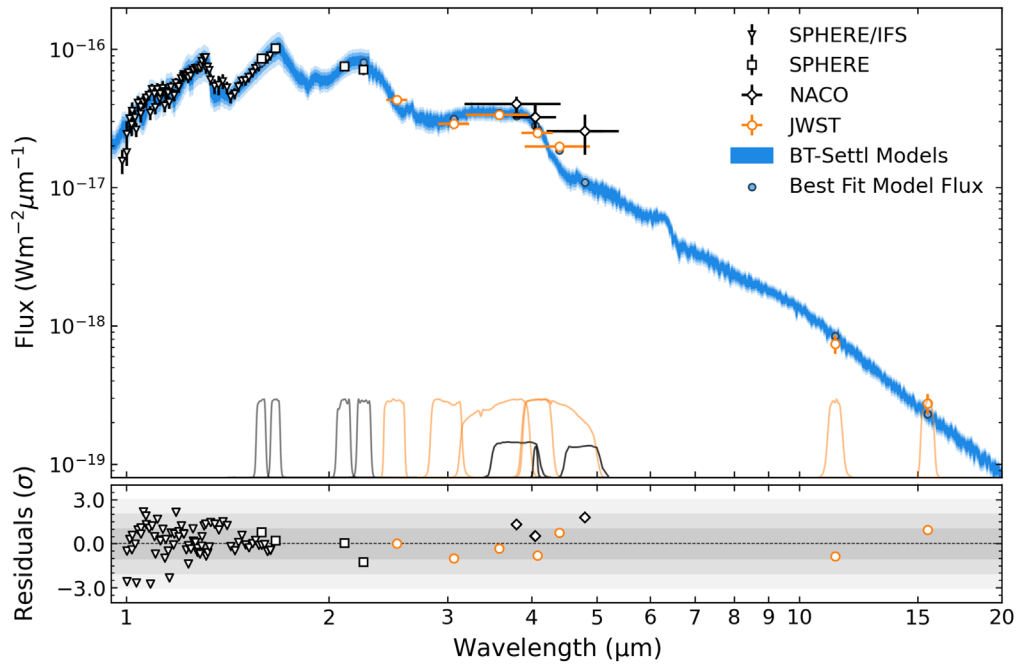


Figure 9. All existing spectroscopic and photometric observations of HIP 65426b as obtained from SPHERE/IFS (triangles), SPHERE/IRDIS (squares), NaCo (diamonds), and JWST (circles). Top: Data are plotted alongside the 1σ , 2σ , and 3σ confidence intervals obtained from fitting to a collection of BT-SETTL atmospheric forward models (blue shaded regions), and the model values in the photometric bandpasses (small blue circles). At 3σ , the best-fit models occupy parameter ranges of $T_{\text{eff}} = 1624_{-15}^{+16}$ K, $\log(g) = 3.88_{-0.08}^{+0.08}$ dex, and $R = 1.06_{-0.05}^{+0.05} R_{\text{Jup}}$. Also plotted are the normalized filter throughput profiles for all photometric observations, with the NaCo throughputs scaled by a factor of 2 to improve clarity. Bottom: Residuals of each data point relative to the best-fit model in addition to 1σ , 2σ , and 3σ regions (gray shading).

luminosity fraction ranges from 61% to 89%, dependent on the adopted model atmosphere.

5.4. Estimates of Mass and Other Companion Properties from Hot-start Evolutionary Models

The mass of HIP 65426b is estimated using a method similar to that described in Dupuy & Liu (2017). We first built an interpolated grid of model luminosities as a function of age and mass, with 10,000 equally spaced age values spanning from 5 to 30 Myr and 10,000 equally spaced mass values spanning from 0.3 to $21 M_{\text{Jup}}$ using `scipy.interpolate.griddata` with cubic interpolation in Python. We adopted an age for HIP 65426b of 14 ± 4 Myr based on the Lower Centaurus-Crux age given in Chauvin et al. (2017) and a measured bolometric luminosity uniformly distributed between $\log(L_{\text{bol}}/L_{\odot}) = -4.14$ and -4.31 from the previous section.

We then generated 1×10^6 samples of age and mass from a Gaussian distribution in age around 14 Myr, with $\sigma = 4$ Myr, and a uniform distribution in mass from 0.3 to $21 M_{\text{Jup}}$. For each sample of age and mass, we then look up the corresponding model luminosity from the interpolated grid of model luminosities. For each sample of age, mass, we accept the sample if the corresponding model luminosity is within the measured range of uniformly distributed bolometric luminosities, and reject the sample if it lies outside this range.

We implemented this procedure using the hybrid cloud grid from Saumon & Marley (2008). Given that this is a dusty, young red object, we expect the Saumon & Marley (2008) models, which take clouds into account, to provide the most reliable estimates of the properties of these objects among the model choices available. To sample the corresponding effective temperatures, surface gravities, and radii corresponding to our accepted mass values, we built interpolated grids of model

effective temperatures, surface gravities, and radii with the same spacing in age and mass as for the interpolated grid of luminosities, then looked up the corresponding property in the appropriate table for each accepted age, mass sample. Histograms of the final set of accepted masses, effective temperatures, surface gravities, and radii for each model are shown in Figure 10. The best value of each parameter was taken as the median of the accepted distribution, with error bars given by the 68% confidence interval as calculated from the histogram of each distribution. We found a mass of $7.1 \pm 1.2 M_{\text{Jup}}$, radius of $1.44 \pm 0.03 R_{\text{Jup}}$ (which therefore imply a surface gravity $\log(g) = 3.93_{-0.09}^{+0.07}$), and effective temperature $T_{\text{eff}} = 1283_{-31}^{+25}$ K.

5.5. Atmospheric Forward Model Comparison

To explore the atmospheric properties of HIP 65426b, we performed a forward modeling analysis using the tool FORMoSA (Petruš et al. 2020), which compares spectroscopic and/or photometric data with grids of precomputed synthetic spectra. The code is based on the nested sampling algorithm (Skilling 2004), a Bayesian inversion method that allows a global exploration of the parameter space provided by the grid. In this work, we limited our analysis to the BT-SETTL grid (CIFIST version; Allard et al. 2012; Baraffe et al. 2015) that accounts for convection using mixing-length theory, and works at hydrostatic, radiative-convective, and chemical equilibrium.

For the fit, we used a data set composed of the low-resolution spectra ($R_{\lambda} \sim 54$) between 1.00 and $1.65 \mu\text{m}$ provided by VLT/SPHERE-IFS (Chauvin et al. 2017), VLT/SPHERE-IRDIS H_2 ($1.58 \mu\text{m}$), H_3 ($1.66 \mu\text{m}$), K_1 ($2.11 \mu\text{m}$), and K_2 ($2.25 \mu\text{m}$) photometry (Cheetham et al. 2019), NaCo L' ($3.77 \mu\text{m}$), NB4.05 ($4.06 \mu\text{m}$), and M' ($4.76 \mu\text{m}$) photometry, and our new JWST NIRCcam and MIRI photometry. We first

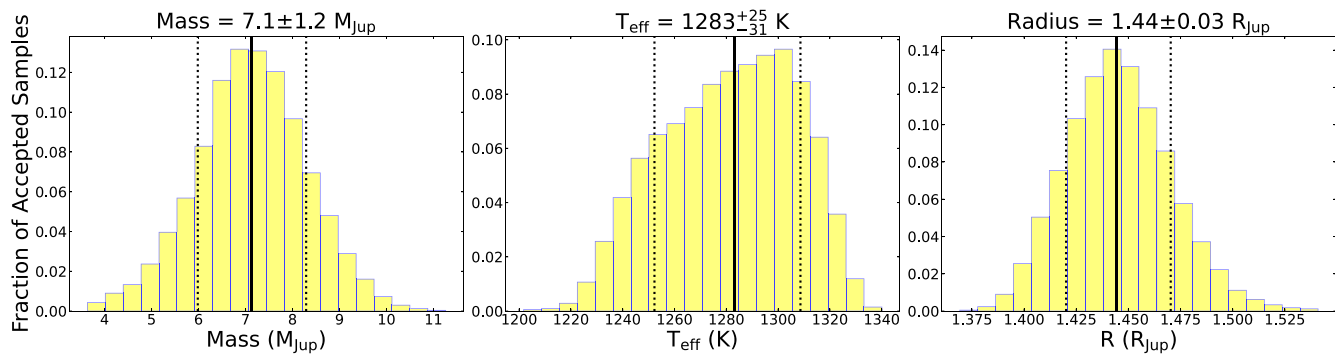


Figure 10. Histograms of the final sets of accepted model properties for the hybrid cloud grid from Saumon & Marley (2008). The median value for each property is shown as a solid black line, with the 68% confidence region falling between the two dotted black lines.

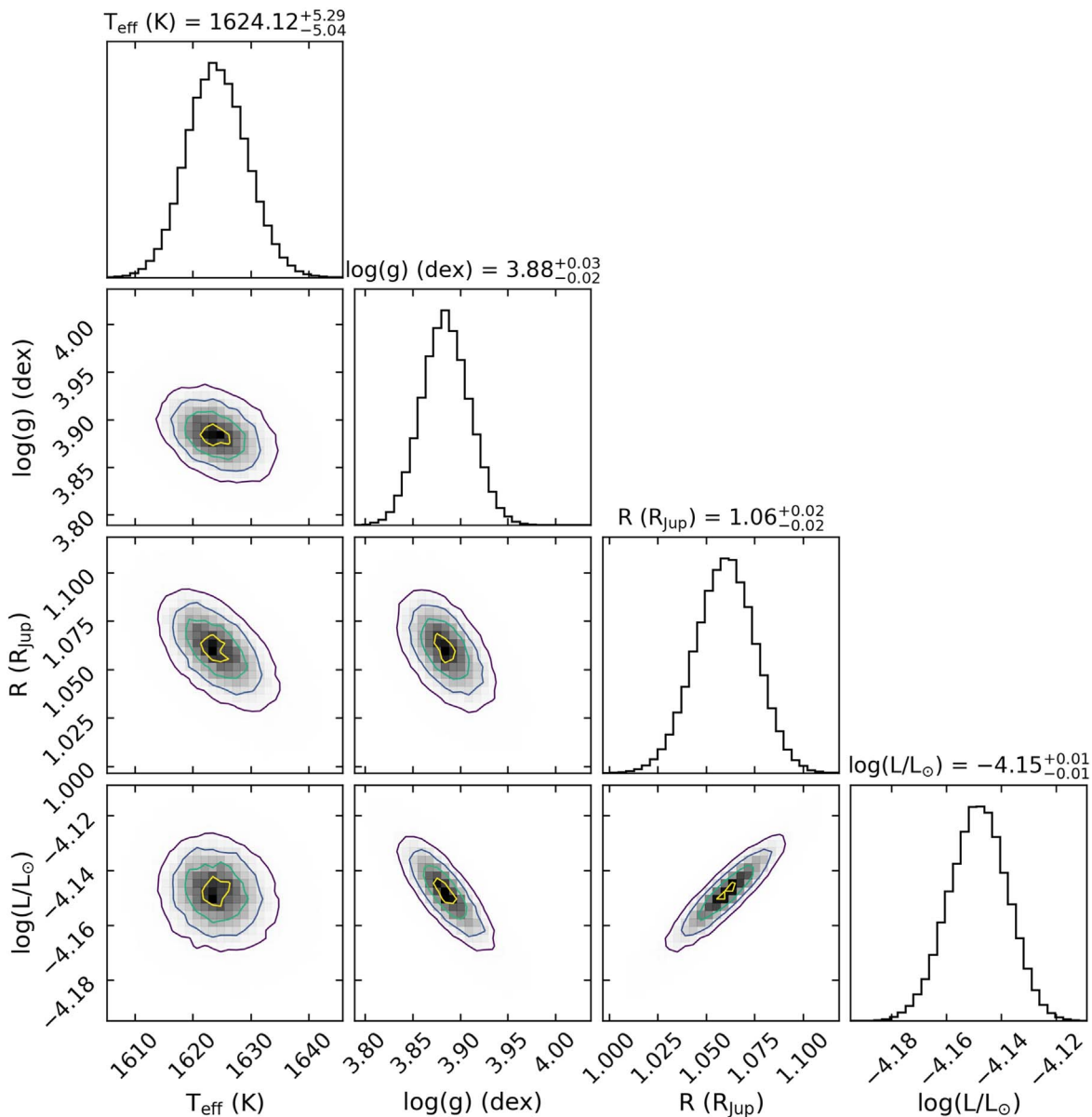


Figure 11. Posterior distributions for the BT–Settl atmospheric model fitting to both JWST and VLT/SPHERE observations of HIP 65426b. Best-fit values and 1σ uncertainties are indicated; however, these should be interpreted as the model phase space that fits these data, and not the precision to which these properties can be empirically measured.

adapted the BT-SETTL synthetic spectra to our data by reducing their spectral resolution to that of SPHERE-IFS and calculating the synthetic photometric flux at each bandpass using throughputs as obtained from `spaceKLIP` for the JWST data, and from the SVO filter service for all other data⁷⁹ (Rodrigo et al. 2012; Rodrigo & Solano 2020). We then defined flat priors on the T_{eff} and the $\log(g)$ according to the limits of the grid, and applied nested sampling to estimate the posterior distributions of these two parameters. We also add the radius, R , to the list of the parameters explored by the nested sampling. At each iteration, a radius is picked randomly (uniform prior), and a dilution factor $C_K = (R/d)^2$ is calculated and multiplied to the model, where d is the distance to the object (107.49 pc).

The best-fit models to our data combined with the existing SPHERE and NaCo data are displayed in Figure 9, alongside posteriors in Figure 11. We estimate $T_{\text{eff}} = 1624^{+16}_{-15}$ K, $\log(g) = 3.88^{+0.08}_{-0.08}$ dex, and $R = 1.06^{+0.05}_{-0.05} R_{\text{Jup}}$. From the T_{eff} and the radius, we apply the Stefan–Boltzmann law and estimate a bolometric luminosity of $\log(L_{\text{bol}}/L_{\odot}) = -4.15^{+0.03}_{-0.03}$, and from the $\log(g)$ and R , we estimate a mass of $M = 3.29 \pm 0.33 M_{\text{Jup}}$. By comparing the integrated flux of the best-fit model across all wavelengths, and the integrated flux between the shortest- and longest-wavelength observations, we determine that these observations span $\sim 97\%$ of HIP 65426b’s luminous range. These results are also in agreement with a similar BT-SETTL model fitting procedure to VLT/SINFONI data of HIP 65426b (see Petrus et al. 2021). The uncertainties of all parameters are given at 3σ ; however, we emphasize that they do not necessarily describe our confidence in the true planetary properties and are better considered as the model phase space that best fits our data.

The precision on these measurements is primarily driven by the SPHERE/IFS data; however, we do note some differences that result from the addition of the JWST data. Specifically, when fitting just the SPHERE and NaCo data in isolation, we obtain $T_{\text{eff}} = 1619^{+18}_{-17}$ K, $\log(g) = 3.85^{+0.10}_{-0.09}$ dex, $R = 1.10^{+0.09}_{-0.09} R_{\text{Jup}}$, and $\log(L_{\text{bol}}/L_{\odot}) = -4.12^{+0.06}_{-0.06}$, again with uncertainties given at 3σ . Therefore, the JWST data improve the precision of the radius and bolometric luminosity by a factor of ~ 2 , but do not significantly improve the precision on the temperature and surface gravity.

The atmospheric forward model fit yields a luminosity within the bolometric luminosity range of -4.14 to -4.31 that was found from combining SED measurements with models in the regions not covered by the SED. However, the effective temperatures and radii found using the atmospheric forward model are considerably in tension with predictions from evolutionary model fits to the measured bolometric luminosity range (see Section 5.4). In particular, to obtain similar bolometric luminosity values, the forward models favor higher effective temperatures (~ 1600 K) and smaller radii ($\sim 1.06 R_{\text{Jup}}$) compared to the evolutionary models (~ 1300 K, $\sim 1.44 R_{\text{Jup}}$). In fact, the atmospheric forward model used here corresponds to an unphysically small radius for an exoplanet that may still be contracting at these young ages. Thus, we consider the effective temperature and radius predictions from the evolutionary models to be more robust here.

The tension we find between the atmospheric models and evolutionary models is well-documented in the community;

atmospheric models have a long history of requiring unphysically small radii and high effective temperatures to fit spectroscopy (see, e.g., Marois et al. 2008; Patience et al. 2012). This stems from the different approaches and fundamental parameters underpinning evolutionary and atmospheric modeling techniques.

Atmospheric models produce model spectra as a function of effective temperature, T_{eff} , surface gravity, g , and composition, irrespective of the mass or age of the object modeled. When fitting atmospheric model spectra to observed spectra, the value of the radius necessary to produce the observed luminosity of the object can be derived if the distance to the object is known. From the radius and the best-fit model surface gravity, a mass value can be derived as well. However, these are not fundamental parameters of the model, but rather extrapolated quantities.

In contrast, evolutionary models couple a similar atmospheric model with a stellar-like interior model, solving for hydrostatic equilibrium and mass conservation, and assuming conservation of energy in shells within the planet (Saumon & Marley 2008). The interior model has fundamental parameters of mass and age; running the model until radiative–convective equilibrium is reached yields a bolometric luminosity and radius. Mass and radius here are then properties of the model, as opposed to the case of the atmospheric models where they are derived quantities dependent in particular on the fit for T_{eff} .

When fitting evolutionary models to observations, we fit directly to the bolometric luminosity. In this work, the bolometric luminosity is measured to very high accuracy, as we are integrating over many wavelength bins. Thus, we find a robust fit to other fundamental properties such as mass, surface gravity, and T_{eff} from evolutionary models. However, if we considered the “best-fit” model spectrum corresponding to the parameters (T_{eff} , $\log(g)$) of the best evolutionary model, it would poorly fit the observed spectrum. In contrast, the atmospheric model fits to the spectra involve directly fitting over many wavelength bins. Uncertainties in cloud parameterization in current models push these fits to higher temperatures to explain the observed spectral features; as a result, to balance out to the measured luminosity of the object at its artificially high T_{eff} , the radius derived from the spectral fit is pushed to implausibly low values. As a consequence of the small radius, the mass estimate from the atmospheric models is also unphysically low.

Further JWST observations across a broad diversity of exoplanets and/or brown dwarfs will be able to empirically constrain these model discrepancies as a function of properties such as temperature, mass, and age, and may in turn uncover their precise origin and extent. Until then, the competing benefits and drawbacks between atmospheric and evolutionary mean that they are best considered in tandem as opposed to in isolation.

5.6. Future Work

There is a range of additional investigation that can be performed on the data presented here that is worth highlighting, but ultimately falls outside the scope of this work.

Most importantly, it is possible to perform the atmospheric forward model fitting procedure shown here in Section 5.5 with a wide range of state-of-the-art models (e.g., ATMO, Tremblin et al. 2015; Phillips et al. 2020; Exo-REM, Charnay et al. 2018; Sonora, Karalidi et al. 2021), each with their own treatment for

⁷⁹ <http://svo2.cab.inta-csic.es/theory/fps/>

the effects of clouds and atmospheric chemistry. Additionally, atmospheric fitting can also be performed using retrieval techniques (e.g., Mollière et al. 2020; Gonzales et al. 2021). Divergences in the measured planetary properties between these models are expected, and a more complete analysis in the context of the relative assumptions of each model will greatly improve our understanding of the true properties of HIP 65426b.

The precision of the 3–5 μm data may be sufficient to provide constraints on the relative atmospheric abundances of CH_4 and CO, which can be impacted by disequilibrium chemistry (Zahnle & Marley 2014; Miles et al. 2020). The F1140C photometry falls slightly under the best-fit model, albeit only at $\sim 1\sigma$, and may be indicative of absorption by small silicate dust grains (Cushing et al. 2006; Suárez & Metchev 2022; Miles et al. 2023). Similarly, the F1550C photometry falls $\sim 1\sigma$ above the best-fit model, and may be sensitive to circumplanetary disk emission (Sterzik et al. 2004; Stolker et al. 2020a).

6. Conclusion

In this work, we present the first-ever scientific observations using the JWST high-contrast imaging modes of both NIRCcam from 2 to 5 μm and MIRI from 11 to 16 μm . The known exoplanet companion, HIP 65426b, is clearly detected in all seven observational filters, representing the first-ever direct detection of an exoplanet beyond 5 μm . These observations provide a variety of insights into (a) the performance and best practices of JWST high-contrast imaging and (b) the properties of the HIP 65426b system, which we summarize below:

1. *Contrast*: JWST is exceeding its anticipated contrast performance for both NIRCcam and MIRI coronagraphy by up to a factor of 10 in the contrast-limited regime (see Section 4.1). For the contrasts achieved, we are sensitive to sub-Jupiter companions with masses as small as $0.3M_{\text{Jup}}$ beyond separations of ~ 100 au. Furthermore, for more optimal targets such as young, nearby M stars, it is highly likely that both NIRCcam and MIRI will be sensitive to sub-Saturn-mass objects beyond ~ 10 au (Carter et al. 2021a).
2. *Subtraction Strategy*: For these data at small separations $< 2''$, the best contrast is obtained using a small-grid dither RDI subtraction strategy for both NIRCcam and MIRI. Additionally, an ADI+RDI subtraction does not significantly improve the measured contrast compared to RDI. For the MIRI F1550C observations in particular, we were unable to recover HIP 65426b using ADI alone. At wider separations, however, the observational efficiency of ADI may make it preferable to RDI. These conclusions may aid future observers in selecting their PSF subtraction strategy, although we emphasize that a clearer understanding of whether they apply under all circumstances will require the analysis of a broader range of JWST coronagraphic observations.
3. *Photometry*: These photometric observations of HIP 65426b provide exquisite sensitivity at a precision of $\sim 7\%$ for NIRCcam and $\sim 16\%$ for MIRI. Furthermore, prior to propagation of the uncertainty in the stellar flux ($\sim 5\%$), and the current absolute flux calibration accuracy (5/15% for NIRCcam/MIRI), the uncertainty in the

measured relative flux is even smaller, at $\sim 2\%$, for both NIRCcam and MIRI. These measurements are a significant step forward from ground-based observations from 3–5 μm , which have comparative uncertainties of $\sim 13\%$ – 32% for HIP 65426b, and they are restricted to particular wavelength regions, due to telluric contamination. With this improved precision, we will be able to constrain directly imaged exoplanet atmospheres in much greater detail, in addition to more complex effects such as variability, disequilibrium chemistry, and the emission of circumplanetary material.

4. *Atmospheric Model Fitting*: Using a BT-SETTL atmospheric forward model, we are able to fit all data, in addition to the majority of ground-based observations to within 2σ . This agreement provides precise constraints on the $T_{\text{eff}} = 1624_{-15}^{+16}$ K, $\log(g) = 3.88_{-0.08}^{+0.08}$ dex, $R = 1.06_{-0.05}^{+0.05} R_{\text{Jup}}$, and $\log(L_{\text{bol}}/L_{\odot}) = -4.15_{-0.03}^{+0.03}$. Compared to a fit excluding the JWST data, this corresponds to a factor of ~ 2 improvement in the precision of the radius and bolometric luminosity. Despite the excellent model agreement, both the temperature and unphysically small radius are in disagreement with the values obtained from the evolutionary models, further emphasizing a long-standing tension for this class of objects.
5. *Empirical Bolometric Luminosity*: As JWST offers a uniquely broad spectral coverage in comparison to ground-based instruments, we are able to obtain a very precise measurement of the bolometric luminosity of HIP 65426b that is constrained between a $\log(L_{\text{bol}}/L_{\odot}) = -4.14$ to -4.31 , irrespective of the model atmosphere adopted for the wavelengths not covered by observations. In combination with evolutionary models, this provides tight constraints on the properties of HIP 65426b with $M = 7.2 \pm 1.1 M_{\text{Jup}}$, $T_{\text{eff}} = 1283_{-31}^{+25}$ K, and $R = 1.44 \pm 0.03 R_{\text{Jup}}$. Given the achieved sensitivity, similar JWST observations will facilitate this analysis for a broader range of PMCs than ever before, and it will provide comparable constraints on their bolometric luminosities—and therefore their masses. These measurements will in turn be valuable for investigating discrepancies between atmospheric and evolutionary models of exoplanets.

In conclusion, the observations reported here from our ERS program (ERS-01386; Hinkley et al. 2022) demonstrate that JWST provides a transformative opportunity to study exoplanets through high-contrast imaging. Beyond this work, we also highlight existing and future publications from our program of 3–16 μm NIRCcam and MIRI coronagraphy of the circumstellar disk HD 141569 A (M. Millar-Blanchaer et al. 2023, in preparation; E. Choquet et al. 2023, in preparation), NIRSpc and MIRI spectroscopy from 1 to 28 μm of the PMC VHS J1256b (Miles et al. 2023), and NIRISS AMI observations of HIP 65426 at 3.8 μm (S. Ray et al. 2023, in preparation; S. Sallum et al. 2023, in preparation).

Acknowledgments

We are truly grateful for the countless hours that thousands of people have devoted to the design, construction, and commissioning of JWST. A.L.C. acknowledges the significant harm caused to members of the LGBTQIA+ community in the

Department of State and NASA, while under the leadership of James Webb as Under Secretary of State and NASA Administrator, respectively. This project was supported by a grant from STScI (JWST-ERS-01386) under NASA contract NAS5-03127. This work benefited from the 2022 Exoplanet Summer Program in the Other Worlds Laboratory (OWL) at the University of California, Santa Cruz, a program funded by the Heising-Simons Foundation. A.L.C. and this work have greatly benefited from ExoExplorers, which is sponsored by the Exoplanets Program Analysis Group (ExoPAG) and NASA's Exoplanet Exploration Program Office (ExEP). This work has made use of the SPHERE Data Centre, jointly operated by OSUG/IPAG (Grenoble), PYTHEAS/LAM/CeSAM (Marseille), OCA/Lagrange (Nice), Observatoire de Paris/LESIA (Paris), and Observatoire de Lyon/CRAL, and is supported by a grant from Labex OSUG@2020 (Investissements d'avenir-ANR10 LABX56). S.P. acknowledges the support of ANID—Millennium Science Initiative Program—NCN19_171. M.B.o. acknowledges support in France from the French National Research Agency (ANR) through project grant ANR-20-CE31-0012. This project has received funding from the European

Research Council (ERC) under the European Union's Horizon 2020 research and innovation program (COBREX, grant agreement No. 885593; EPIC, grant agreement No. 819155). All the JWST presented in this paper were obtained from the Mikulski Archive for Space Telescopes (MAST) at the Space Telescope Science Institute and can be accessed via DOI: [10.17909/2bdf-3p61](https://doi.org/10.17909/2bdf-3p61). This research has also made use of the NASA Astrophysics Data System Bibliographic services and the Python (Van Rossum & Drake 2009) modules listed below.

Software: NumPy (Harris et al. 2020), matplotlib (Hunter 2007), Astropy (Astropy Collaboration et al. 2013, 2018), SciPy (Virtanen et al. 2020), scikit-image (Van der Walt et al. 2014), synphot (STScI Development Team 2018), emcee (Foreman-Mackey et al. 2013), MultiNest (Feroz et al. 2009; Buchner et al. 2014), PHOENIX (Allard et al. 2012), webbpsf (Perrin et al. 2012, 2014), PanCAKE (Carter et al. 2021b), orbitize! (Blunt et al. 2017, 2020), Exo-DMC (Bonavita et al. 2013; Bonavita 2020), pyKLIP (Wang et al. 2015), spaceKLIP (Kammerer et al. 2022).

Appendix A Subtracted Images

Subtracted images for all NIRCam and MIRI observations are displayed below in Figures 12 and 13.

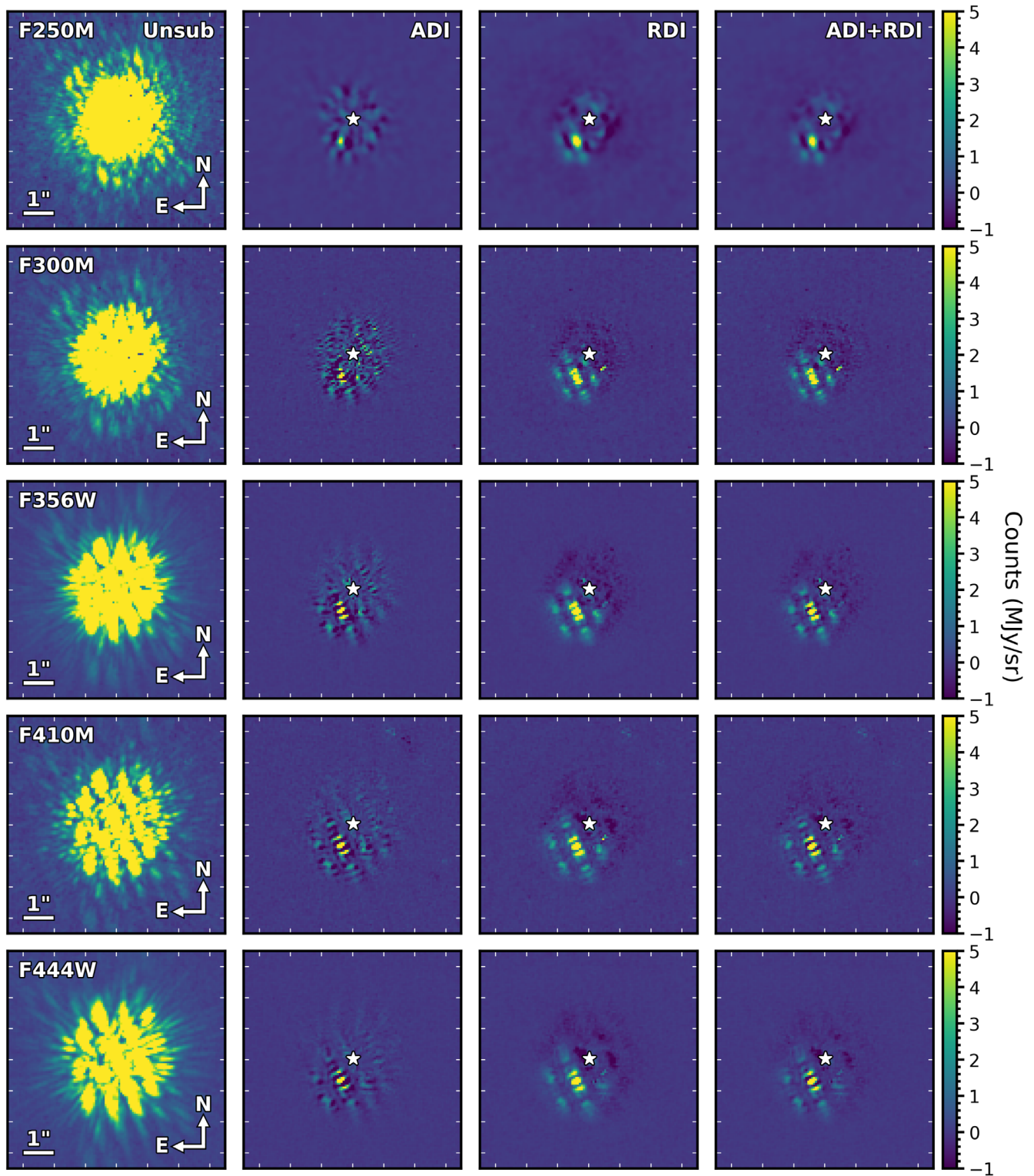


Figure 12. As in Figure 3, except for the NIRCam F250M, F300M, F356W, F410M, and F444W filters. Here, we show subtractions using the maximum number of PCA modes for ADI, RDI, and ADI+RDI, respectively. The F250M subtracted images have been smoothed as described in Section 2.

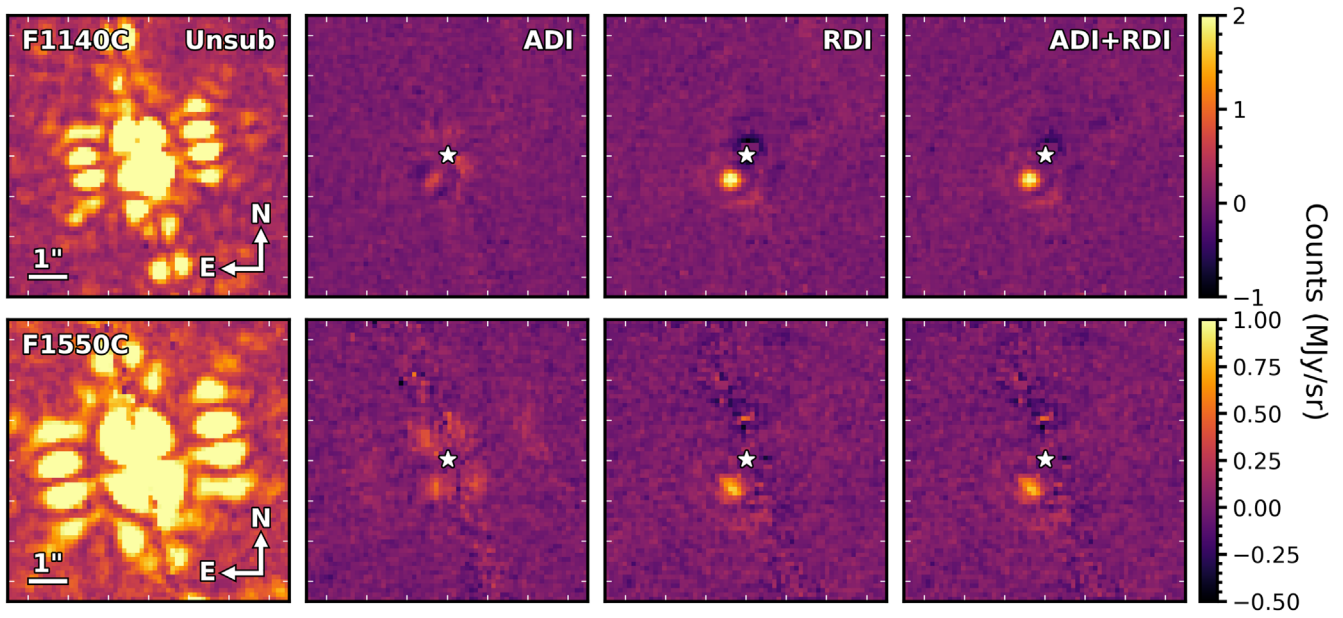


Figure 13. As in Figure 3, except for the MIRI F1140C and F1550C filters. Here, we show subtractions using the maximum number of PCA modes for ADI, RDI, and ADI+RDI, respectively. To aid visual clarity, the subtracted F1550C images are shown with a peak image intensity five times smaller than the unsubtracted image.

Appendix B Contrast Performance

Contrast curves for all observations are displayed below in Figure 14.

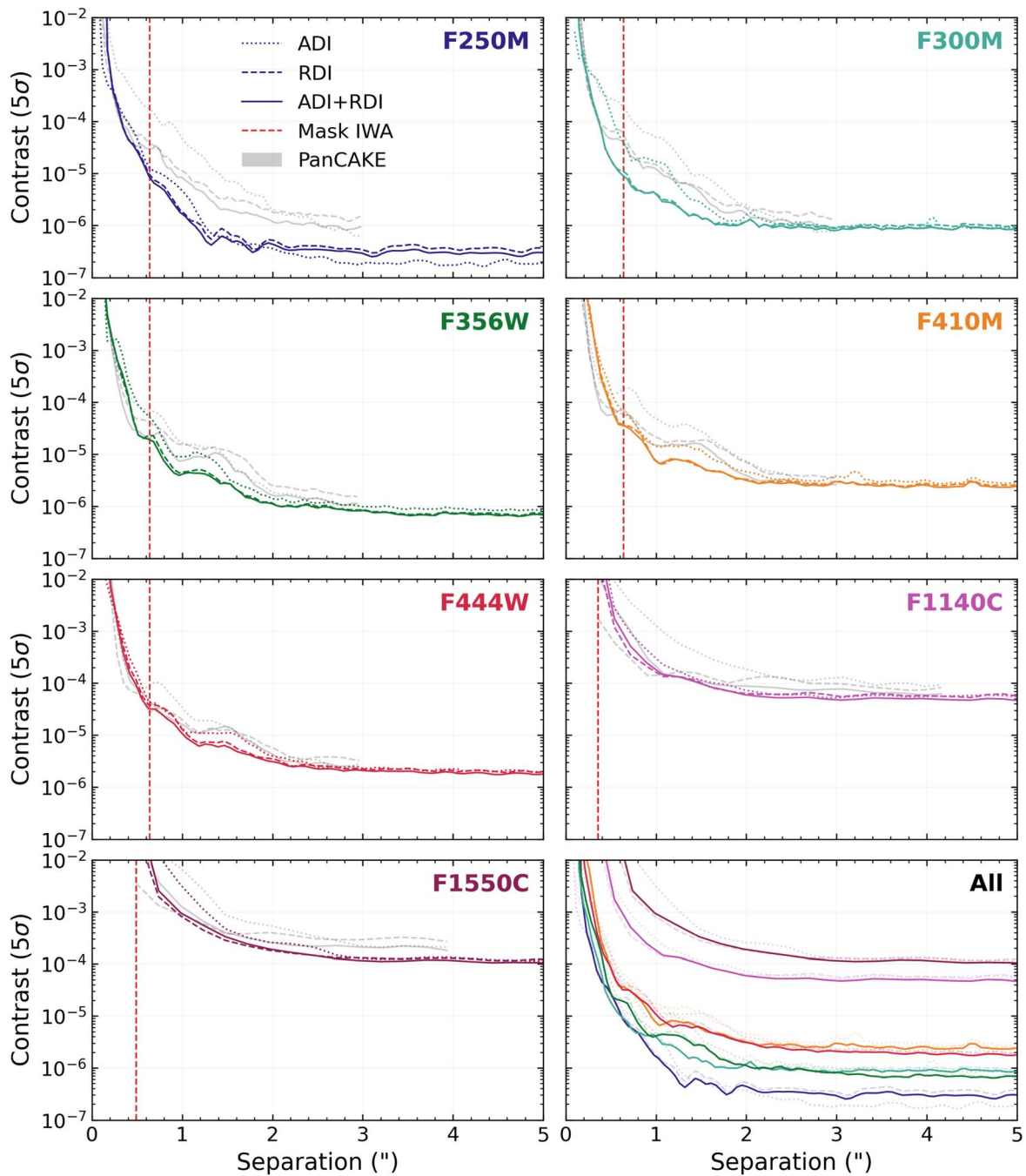


Figure 14. As in Figure 5, but for all used filters. We also plot the equivalent predicted contrast curves for these observations from PanCAKE (gray lines) following Carter et al. (2021b). In every filter, JWST is exceeding its predicted performance.

Appendix C PSF Fitting

Model fits and residuals to the companion HIP 65426b for all filters are displayed below in Figures 15 and 16.

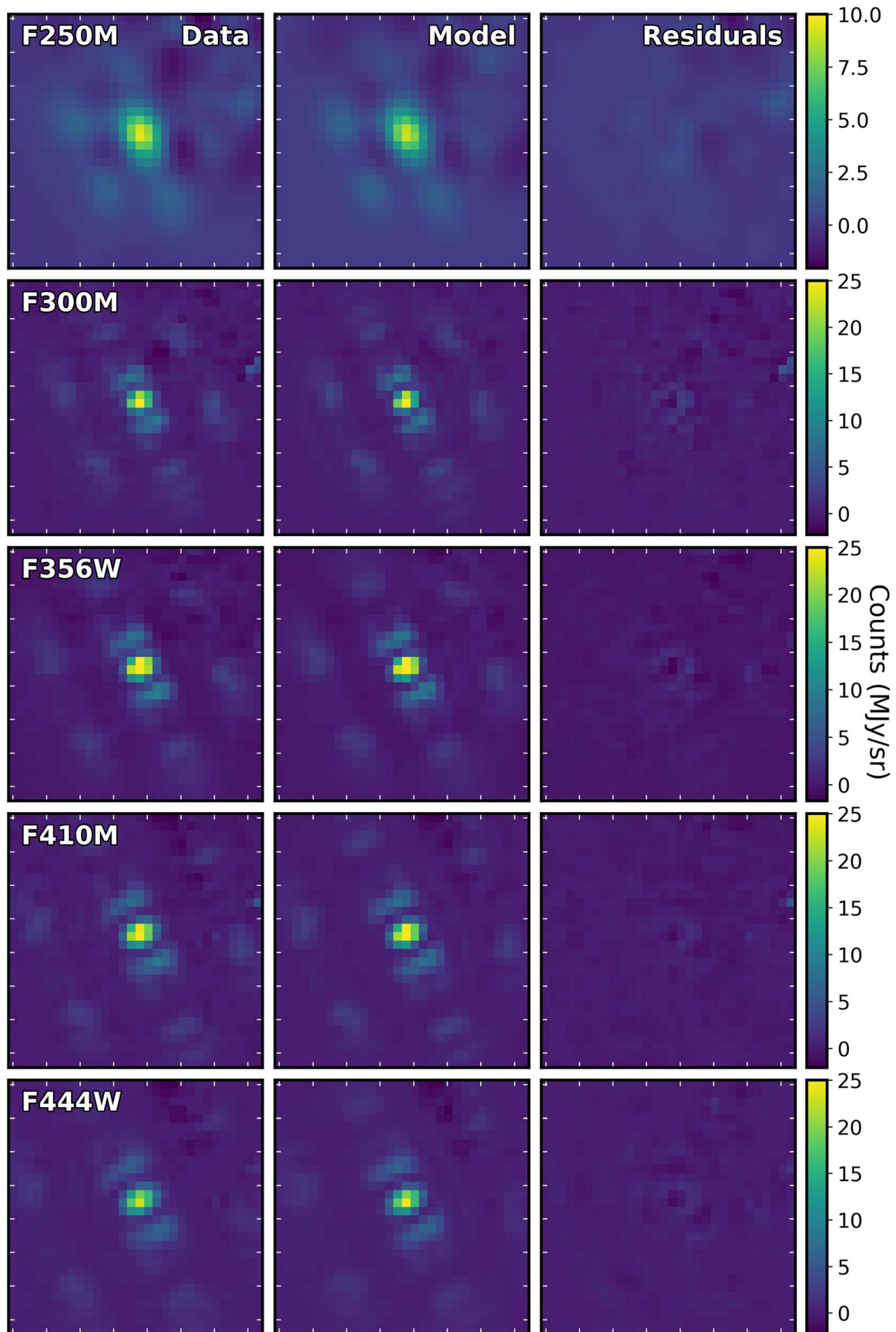


Figure 15. The data (left column), model PSF (middle column), and residuals (right column) for the *spaceKLIP* PSF fitting of the NIRCcam observations of HIP 65426b. Pixel counts are in MJy/sr and are indicated by the color bar on the right-hand side, images are oriented with north upward and north through east counterclockwise, and the image size is 30×30 pixels ($1''.9 \times 1''.9$).

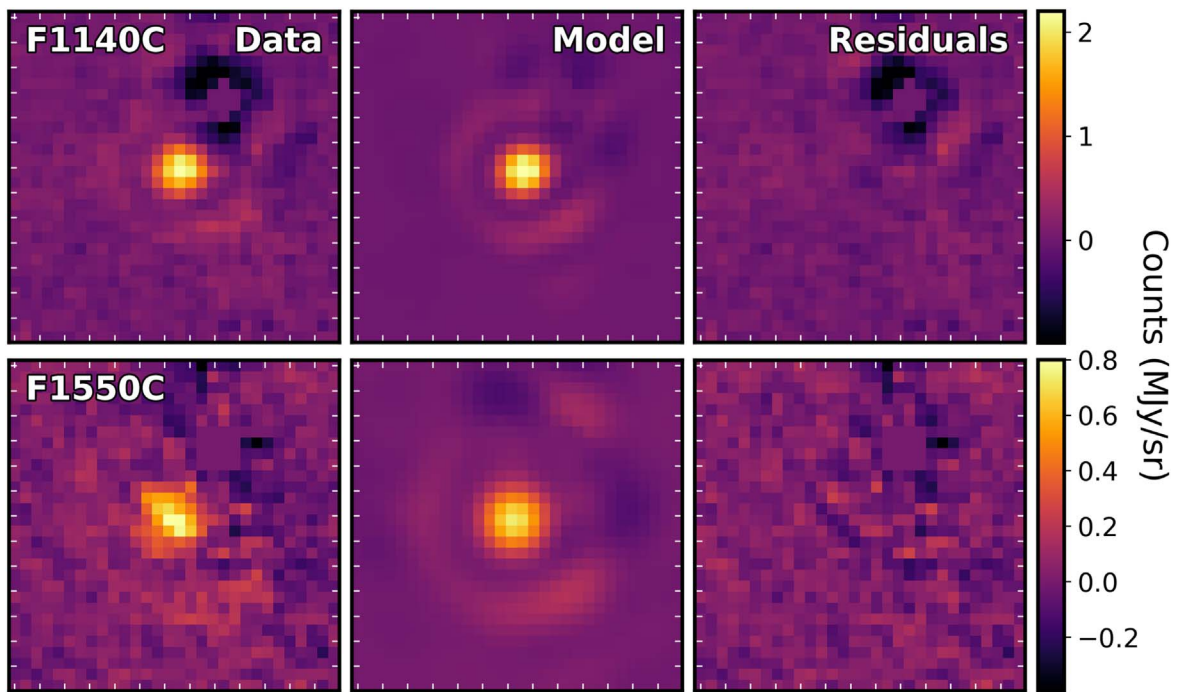


Figure 16. As in Figure 15, but for the MIRI observations. The image size is 30×30 pixels ($3.3 \times 3.3''$).

Appendix D Complementary Photometric Measurements of HIP 65426b

All measurements of HIP 65426b considered during our model fitting process are displayed below in Table 4.

Table 4
Additional Photometric Measurements of HIP 65426b Considered in This Work

Wavelength (μm)	Bandwidth (μm)	Instrument	Band	Flux ($\text{W m}^{-2} \mu\text{m}^{-1}$)	References
1.002	0.011	SPHERE/IFS	YJ	$(2.434 \pm 0.569) \times 10^{-17}$	1
1.011	0.011	SPHERE/IFS	YJ	$(3.155 \pm 0.670) \times 10^{-17}$	1
1.021	0.011	SPHERE/IFS	YJ	$(3.564 \pm 0.575) \times 10^{-17}$	1
1.030	0.011	SPHERE/IFS	YJ	$(3.199 \pm 0.428) \times 10^{-17}$	1
1.040	0.011	SPHERE/IFS	YJ	$(4.095 \pm 0.482) \times 10^{-17}$	1
1.050	0.011	SPHERE/IFS	YJ	$(3.829 \pm 0.435) \times 10^{-17}$	1
1.060	0.011	SPHERE/IFS	YJ	$(4.154 \pm 0.489) \times 10^{-17}$	1
1.070	0.011	SPHERE/IFS	YJ	$(4.456 \pm 0.521) \times 10^{-17}$	1
1.081	0.011	SPHERE/IFS	YJ	$(4.679 \pm 0.432) \times 10^{-17}$	1
1.091	0.011	SPHERE/IFS	YJ	$(5.143 \pm 0.483) \times 10^{-17}$	1
1.102	0.011	SPHERE/IFS	YJ	$(4.746 \pm 0.543) \times 10^{-17}$	1
1.112	0.011	SPHERE/IFS	YJ	$(5.127 \pm 0.576) \times 10^{-17}$	1
1.123	0.011	SPHERE/IFS	YJ	$(4.775 \pm 0.641) \times 10^{-17}$	1
1.133	0.011	SPHERE/IFS	YJ	$(5.228 \pm 0.682) \times 10^{-17}$	1
1.144	0.011	SPHERE/IFS	YJ	$(4.982 \pm 0.609) \times 10^{-17}$	1
1.154	0.011	SPHERE/IFS	YJ	$(4.821 \pm 0.519) \times 10^{-17}$	1
1.165	0.011	SPHERE/IFS	YJ	$(5.324 \pm 0.486) \times 10^{-17}$	1
1.175	0.011	SPHERE/IFS	YJ	$(4.739 \pm 0.453) \times 10^{-17}$	1
1.186	0.011	SPHERE/IFS	YJ	$(5.709 \pm 0.477) \times 10^{-17}$	1
1.196	0.011	SPHERE/IFS	YJ	$(5.291 \pm 0.415) \times 10^{-17}$	1
1.206	0.011	SPHERE/IFS	YJ	$(6.155 \pm 0.471) \times 10^{-17}$	1
1.217	0.011	SPHERE/IFS	YJ	$(6.586 \pm 0.490) \times 10^{-17}$	1
1.227	0.011	SPHERE/IFS	YJ	$(6.431 \pm 0.500) \times 10^{-17}$	1
1.237	0.011	SPHERE/IFS	YJ	$(6.203 \pm 0.483) \times 10^{-17}$	1
1.247	0.011	SPHERE/IFS	YJ	$(6.409 \pm 0.477) \times 10^{-17}$	1
1.257	0.011	SPHERE/IFS	YJ	$(7.100 \pm 0.483) \times 10^{-17}$	1
1.266	0.011	SPHERE/IFS	YJ	$(7.289 \pm 0.502) \times 10^{-17}$	1
1.276	0.011	SPHERE/IFS	YJ	$(7.344 \pm 0.504) \times 10^{-17}$	1
1.285	0.011	SPHERE/IFS	YJ	$(7.315 \pm 0.499) \times 10^{-17}$	1
1.294	0.011	SPHERE/IFS	YJ	$(8.215 \pm 0.543) \times 10^{-17}$	1
1.303	0.011	SPHERE/IFS	YJ	$(8.701 \pm 0.543) \times 10^{-17}$	1
1.312	0.011	SPHERE/IFS	YJ	$(8.731 \pm 0.580) \times 10^{-17}$	1
1.321	0.011	SPHERE/IFS	YJ	$(7.450 \pm 0.594) \times 10^{-17}$	1
1.329	0.011	SPHERE/IFS	YJ	$(7.073 \pm 0.583) \times 10^{-17}$	1
0.987	0.019	SPHERE/IFS	YJH	$(1.556 \pm 0.312) \times 10^{-17}$	1
1.002	0.019	SPHERE/IFS	YJH	$(1.791 \pm 0.355) \times 10^{-17}$	1
1.018	0.019	SPHERE/IFS	YJH	$(2.855 \pm 0.510) \times 10^{-17}$	1
1.034	0.019	SPHERE/IFS	YJH	$(2.615 \pm 0.305) \times 10^{-17}$	1
1.051	0.019	SPHERE/IFS	YJH	$(3.394 \pm 0.442) \times 10^{-17}$	1
1.068	0.019	SPHERE/IFS	YJH	$(4.239 \pm 0.456) \times 10^{-17}$	1
1.086	0.019	SPHERE/IFS	YJH	$(3.472 \pm 0.407) \times 10^{-17}$	1
1.104	0.019	SPHERE/IFS	YJH	$(3.802 \pm 0.415) \times 10^{-17}$	1
1.122	0.019	SPHERE/IFS	YJH	$(4.403 \pm 0.504) \times 10^{-17}$	1
1.140	0.019	SPHERE/IFS	YJH	$(3.906 \pm 0.397) \times 10^{-17}$	1
1.159	0.019	SPHERE/IFS	YJH	$(4.132 \pm 0.422) \times 10^{-17}$	1
1.178	0.019	SPHERE/IFS	YJH	$(4.641 \pm 0.452) \times 10^{-17}$	1
1.197	0.019	SPHERE/IFS	YJH	$(5.368 \pm 0.544) \times 10^{-17}$	1
1.216	0.019	SPHERE/IFS	YJH	$(6.356 \pm 0.573) \times 10^{-17}$	1
1.235	0.019	SPHERE/IFS	YJH	$(6.763 \pm 0.602) \times 10^{-17}$	1
1.255	0.019	SPHERE/IFS	YJH	$(7.107 \pm 0.622) \times 10^{-17}$	1
1.274	0.019	SPHERE/IFS	YJH	$(7.228 \pm 0.630) \times 10^{-17}$	1
1.294	0.019	SPHERE/IFS	YJH	$(7.599 \pm 0.668) \times 10^{-17}$	1
1.314	0.019	SPHERE/IFS	YJH	$(7.296 \pm 0.648) \times 10^{-17}$	1
1.333	0.019	SPHERE/IFS	YJH	$(6.046 \pm 0.577) \times 10^{-17}$	1
1.353	0.019	SPHERE/IFS	YJH	$(5.400 \pm 0.649) \times 10^{-17}$	1




Table 4
(Continued)





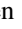


Wavelength (μm)	Bandwidth (μm)	Instrument	Band	Flux ($\text{W m}^{-2} \mu\text{m}^{-1}$)	References
1.372	0.019	SPHERE/IFS	YJH	$(5.523 \pm 0.872) \times 10^{-17}$	1
1.391	0.019	SPHERE/IFS	YJH	$(5.875 \pm 0.729) \times 10^{-17}$	1
1.411	0.019	SPHERE/IFS	YJH	$(5.285 \pm 0.550) \times 10^{-17}$	1
1.430	0.019	SPHERE/IFS	YJH	$(4.516 \pm 0.460) \times 10^{-17}$	1
1.449	0.019	SPHERE/IFS	YJH	$(4.768 \pm 0.439) \times 10^{-17}$	1
1.467	0.019	SPHERE/IFS	YJH	$(5.374 \pm 0.484) \times 10^{-17}$	1
1.486	0.019	SPHERE/IFS	YJH	$(5.888 \pm 0.506) \times 10^{-17}$	1
1.504	0.019	SPHERE/IFS	YJH	$(5.927 \pm 0.498) \times 10^{-17}$	1
1.522	0.019	SPHERE/IFS	YJH	$(6.259 \pm 0.519) \times 10^{-17}$	1
1.539	0.019	SPHERE/IFS	YJH	$(6.778 \pm 0.561) \times 10^{-17}$	1
1.556	0.019	SPHERE/IFS	YJH	$(7.318 \pm 0.605) \times 10^{-17}$	1
1.573	0.019	SPHERE/IFS	YJH	$(7.560 \pm 0.624) \times 10^{-17}$	1
1.589	0.019	SPHERE/IFS	YJH	$(8.037 \pm 0.665) \times 10^{-17}$	1
1.605	0.019	SPHERE/IFS	YJH	$(8.497 \pm 0.706) \times 10^{-17}$	1
1.621	0.019	SPHERE/IFS	YJH	$(8.579 \pm 0.715) \times 10^{-17}$	1
1.636	0.019	SPHERE/IFS	YJH	$(9.011 \pm 0.762) \times 10^{-17}$	1
1.593	0.055	SPHERE/IRDIS	H2	$(8.569 \pm 0.383) \times 10^{-17}$	1
1.667	0.056	SPHERE/IRDIS	H3	$(10.129 \pm 0.564) \times 10^{-17}$	1
2.110	0.102	SPHERE/IRDIS	K1	$(7.500 \pm 0.600) \times 10^{-17}$	1
2.251	0.109	SPHERE/IRDIS	K2	$(7.100 \pm 0.600) \times 10^{-17}$	1
3.800	0.620	NACO	L'	$(4.010 \pm 0.542) \times 10^{-17}$	2,3
4.051	0.020	NACO	NB4.05	$(3.220 \pm 0.780) \times 10^{-17}$	3
4.780	0.590	NACO	M'	$(2.549 \pm 0.820) \times 10^{-17}$	2, 3

Note. For the L' - and M' -band photometry, we considered the average of the measurements reported in Cheetham et al. (2019) and Stolker et al. (2020b), but kept the largest error bars.

References. (1) Chauvin et al. 2017; (2) Cheetham et al. 2019; (3) Stolker et al. 2020b.

ORCID iDs

Aarynn L. Carter  <https://orcid.org/0000-0001-5365-4815>
 Sasha Hinkley  <https://orcid.org/0000-0001-8074-2562>
 Jens Kammerer  <https://orcid.org/0000-0003-2769-0438>
 Andrew Skemer  <https://orcid.org/0000-0001-6098-3924>
 Beth A. Biller  <https://orcid.org/0000-0003-4614-7035>
 Jarron M. Leisenring  <https://orcid.org/0000-0002-0834-6140>
 Maxwell A. Millar-Blanchaer  <https://orcid.org/0000-0001-6205-9233>
 Simon Petrus  <https://orcid.org/0000-0003-0331-3654>
 Jordan M. Stone  <https://orcid.org/0000-0003-0454-3718>
 Kimberly Ward-Duong  <https://orcid.org/0000-0002-4479-8291>
 Jason J. Wang  <https://orcid.org/0000-0003-0774-6502>
 Julien H. Girard  <https://orcid.org/0000-0001-8627-0404>
 Dean C. Hines  <https://orcid.org/0000-0003-4653-6161>
 Marshall D. Perrin  <https://orcid.org/0000-0002-3191-8151>
 William O. Balmer  <https://orcid.org/0000-0001-6396-8439>
 Mariangela Bonavita  <https://orcid.org/0000-0002-7520-8389>
 Mickael Bonnefoy  <https://orcid.org/0000-0001-5579-5339>
 Gael Chauvin  <https://orcid.org/0000-0003-4022-8598>
 Elodie Choquet  <https://orcid.org/0000-0002-9173-0740>
 Valentin Christiaens  <https://orcid.org/0000-0002-0101-8814>
 Camilla Danielski  <https://orcid.org/0000-0002-3729-2663>
 Grant M. Kennedy  <https://orcid.org/0000-0001-6831-7547>
 Elisabeth C. Matthews  <https://orcid.org/0000-0003-0593-1560>

Brittany E. Miles  <https://orcid.org/0000-0002-5500-4602>
 Polychronis Patapis  <https://orcid.org/0000-0001-8718-3732>
 Shrishmoy Ray  <https://orcid.org/0000-0003-2259-3911>
 Emily Rickman  <https://orcid.org/0000-0003-4203-9715>
 Steph Sallum  <https://orcid.org/0000-0001-6871-6775>
 Karl R. Stapelfeldt  <https://orcid.org/0000-0002-2805-7338>
 Niall Whiteford  <https://orcid.org/0000-0001-8818-1544>
 Yifan Zhou  <https://orcid.org/0000-0003-2969-6040>
 Olivier Absil  <https://orcid.org/0000-0002-4006-6237>
 Anthony Boccaletti  <https://orcid.org/0000-0001-9353-2724>
 Mark Booth  <https://orcid.org/0000-0001-8568-6336>
 Brendan P. Bowler  <https://orcid.org/0000-0003-2649-2288>
 Christine H. Chen  <https://orcid.org/0000-0002-8382-0447>
 Thayne Currie  <https://orcid.org/0000-0002-7405-3119>
 Jonathan J. Fortney  <https://orcid.org/0000-0002-9843-4354>
 Alexandra Z. Greebaum  <https://orcid.org/0000-0002-7162-8036>
 Thomas Henning  <https://orcid.org/0000-0002-1493-300X>
 Kielan K. W. Hoch  <https://orcid.org/0000-0002-9803-8255>
 Markus Janson  <https://orcid.org/0000-0001-8345-593X>
 Paul Kalas  <https://orcid.org/0000-0002-6221-5360>
 Matthew A. Kenworthy  <https://orcid.org/0000-0002-7064-8270>
 Pierre Kervella  <https://orcid.org/0000-0003-0626-1749>
 Adam L. Kraus  <https://orcid.org/0000-0001-9811-568X>
 Michael C. Liu  <https://orcid.org/0000-0003-2232-7664>
 Bruce Macintosh  <https://orcid.org/0000-0003-1212-7538>
 Sebastian Marino  <https://orcid.org/0000-0002-5352-2924>
 Mark S. Marley  <https://orcid.org/0000-0002-5251-2943>
 Christian Marois  <https://orcid.org/0000-0002-4164-4182>

Brenda C. Matthews  <https://orcid.org/0000-0003-3017-9577>
 Dimitri Mawet  <https://orcid.org/0000-0002-8895-4735>
 Michael W. McElwain  <https://orcid.org/0000-0003-0241-8956>
 Stanimir Metchev  <https://orcid.org/0000-0003-3050-8203>
 Michael R. Meyer  <https://orcid.org/0000-0003-1227-3084>
 Paul Molliere  <https://orcid.org/0000-0003-4096-7067>
 Sarah E. Moran  <https://orcid.org/0000-0002-6721-3284>
 Caroline V. Morley  <https://orcid.org/0000-0002-4404-0456>
 Sagnick Mukherjee  <https://orcid.org/0000-0003-1622-1302>
 Eric Pantin  <https://orcid.org/0000-0001-6472-2844>
 Isabel Rebolledo  <https://orcid.org/0000-0002-4388-6417>
 Bin B. Ren  <https://orcid.org/0000-0003-1698-9696>
 Glenn Schneider  <https://orcid.org/0000-0002-4511-5966>
 Malavika Vasist  <https://orcid.org/0000-0002-4511-3602>
 Kadin Worthen  <https://orcid.org/0000-0002-5885-5779>
 Mark C. Wyatt  <https://orcid.org/0000-0001-9064-5598>
 Zackery W. Briesemeister  <https://orcid.org/0000-0002-1764-2494>
 Marta L. Bryan  <https://orcid.org/0000-0002-6076-5967>
 Per Calissendorff  <https://orcid.org/0000-0002-5335-0616>
 Faustine Cantalloube  <https://orcid.org/0000-0002-3968-3780>
 Gabriele Cugno  <https://orcid.org/0000-0001-7255-3251>
 Matthew De Furio  <https://orcid.org/0000-0003-1863-4960>
 Trent J. Dupuy  <https://orcid.org/0000-0001-9823-1445>
 Samuel M. Factor  <https://orcid.org/0000-0002-8332-8516>
 Jacqueline K. Faherty  <https://orcid.org/0000-0001-6251-0573>
 Michael P. Fitzgerald  <https://orcid.org/0000-0002-0176-8973>
 Kyle Franson  <https://orcid.org/0000-0003-4557-414X>
 Eileen C. Gonzales  <https://orcid.org/0000-0003-4636-6676>
 Callie E. Hood  <https://orcid.org/0000-0003-1150-7889>
 Alex R. Howe  <https://orcid.org/0000-0002-4884-7150>
 Masayuki Kuzuhara  <https://orcid.org/0000-0002-4677-9182>
 Kellen Lawson  <https://orcid.org/0000-0002-6964-8732>
 Cecilia Lazzoni  <https://orcid.org/0000-0001-7819-9003>
 Ben W. P. Lew  <https://orcid.org/0000-0003-1487-6452>
 Pengyu Liu  <https://orcid.org/0000-0001-7047-0874>
 Jorge Llop-Sayson  <https://orcid.org/0000-0002-3414-784X>
 Raquel A. Martinez  <https://orcid.org/0000-0001-6301-896X>
 Johan Mazoyer  <https://orcid.org/0000-0002-9133-3091>
 Paulina Palma-Bifani  <https://orcid.org/0000-0002-6217-6867>
 Sascha P. Quanz  <https://orcid.org/0000-0003-3829-7412>
 Jea Adams Redai  <https://orcid.org/0000-0002-4489-3168>
 Matthias Samland  <https://orcid.org/0000-0001-9992-4067>
 Joshua E. Schlieder  <https://orcid.org/0000-0001-5347-7062>
 Motohide Tamura  <https://orcid.org/0000-0002-6510-0681>
 Xianyu Tan  <https://orcid.org/0000-0003-2278-6932>
 Taichi Uyama  <https://orcid.org/0000-0002-6879-3030>
 Arthur Vigan  <https://orcid.org/0000-0002-5902-7828>
 Johanna M. Vos  <https://orcid.org/0000-0003-0489-1528>
 Kevin Wagner  <https://orcid.org/0000-0002-4309-6343>
 Schuyler G. Wolff  <https://orcid.org/0000-0002-9977-8255>
 Marie Ygouf  <https://orcid.org/0000-0001-7591-2731>
 Xi Zhang  <https://orcid.org/0000-0002-8706-6963>

Keming Zhang  <https://orcid.org/0000-0002-9870-5695>
 Zhoujian Zhang  <https://orcid.org/0000-0002-3726-4881>

References

- Adams, J., & Wang, J. 2020, *RNAAS*, 4, 227
 Allard, F., Homeier, D., & Freytag, B. 2012, *RSPTA*, 370, 2765
 Astropy Collaboration, Price-Whelan, A. M., Sipőcz, B. M., et al. 2018, *AJ*, 156, 123
 Astropy Collaboration, Robitaille, T. P., Tollerud, E. J., et al. 2013, *A&A*, 558, A33
 Bagnasco, G., Kolm, M., Ferruit, P., et al. 2007, *Proc. SPIE*, 6692, 66920M
 Baraffe, I., Homeier, D., Allard, F., & Chabrier, G. 2015, *A&A*, 577, A42
 Beichman, C., Ygouf, M., Llop Sayson, J., et al. 2020, *PASP*, 132, 015002
 Beichman, C. A., Mawet, D., Belikov, R., et al. 2021, Searching Our Closest Stellar Neighbor for Planets and Zodiacal Emission, JWST Proposal. Cycle 1, ID. #1618
 Best, W. M. J., Dupuy, T. J., Liu, M. C., Siverd, R. J., & Zhang, Z. 2020, The UltracoolSheet: Photometry, Astrometry, Spectroscopy, and Multiplicity for 3000+ Ultracool Dwarfs and Imaged Exoplanets, v1.0.0, Zenodo, doi:10.5281/zenodo.4169085
 Bezuit, J. L., Vigan, A., Mouillet, D., et al. 2019, *A&A*, 631, A155
 Blunt, S., Nielsen, E. L., De Rosa, R. J., et al. 2017, *AJ*, 153, 229
 Blunt, S., Wang, J. J., Angelo, I., et al. 2020, *AJ*, 159, 89
 Boccaletti, A., Cossou, C., Baudoz, P., et al. 2022, *A&A*, 667, A165
 Boccaletti, A., Lagage, P. O., Baudoz, P., et al. 2015, *PASP*, 127, 633
 Bohlin, R. C., Gordon, K. D., & Tremblay, P. E. 2014, *PASP*, 126, 711
 Bohn, A. J., Kenworthy, M. A., Ginski, C., et al. 2020, *ApJL*, 898, L16
 Böker, T., Arribas, S., Lützendorf, N., et al. 2022, *A&A*, 661, A82
 Bonavita, M. 2020, Exo-DMC: Exoplanet Detection Map Calculator, Astrophysics Source Code Library, ascl:2010.008
 Bonavita, M., Chauvin, G., Desidera, S., et al. 2012, *A&A*, 537, A67
 Bonavita, M., de Mooij, E. J. W., & Jayawardhana, R. 2013, *PASP*, 125, 849
 Bowler, B. P., Blunt, S. C., & Nielsen, E. L. 2020, *AJ*, 159, 63
 Brande, J., Barclay, T., Schlieder, J. E., Lopez, E. D., & Quintana, E. V. 2020, *AJ*, 159, 18
 Buchner, J., Georgakakis, A., Nandra, K., et al. 2014, *A&A*, 564, A125
 Bushouse, H., Eisenhamer, J., Dencheva, N., et al. 2022, JWST Calibration Pipeline, v1.6.2, Zenodo, doi:10.5281/zenodo.6984366
 Carter, A. L., Hinkley, S., Bonavita, M., et al. 2021a, *MNRAS*, 501, 1999
 Carter, A. L., Skemer, A. J. I., Danielski, C., et al. 2021b, *Proc. SPIE*, 11823, 118230H
 Charnay, B., Bézard, B., Baudino, J. L., et al. 2018, *ApJ*, 854, 172
 Chauvin, G., Desidera, S., Lagrange, A.-M., et al. 2017, *A&A*, 605, L9
 Chauvin, G., Lagrange, A. M., Dumas, C., et al. 2004, *A&A*, 425, L29
 Cheetham, A. C., Samland, M., Brems, S. S., et al. 2019, *A&A*, 622, A80
 Chen, C. H., Pecauc, M., Mamajek, E. E., Su, K. Y. L., & Bitner, M. 2012, *ApJ*, 756, 133
 Chilcote, J., Konopacky, Q., De Rosa, R. J., et al. 2020, *Proc. SPIE*, 11447, 114471S
 Currie, T., Biller, B., Lagrange, A.-M., et al. 2022, arXiv:2205.05696
 Cushing, M. C., Roellig, T. L., Marley, M. S., et al. 2006, *ApJ*, 648, 614
 Cutri, R. M., Skrutskie, M. F., van Dyk, S., et al. 2003, The IRSA 2MASS All-Sky Point Source Catalog, NASA/IPAC Infrared Science Archive
 Danielski, C., Baudino, J.-L., Lagage, P.-O., et al. 2018, *AJ*, 156, 276
 Doyon, R., Hutchings, J. B., Beaulieu, M., et al. 2012, *Proc. SPIE*, 8442, 84422R
 Dupuy, T. J., & Liu, M. C. 2017, *ApJS*, 231, 15
 Feroz, F., Hobson, M. P., & Bridges, M. 2009, *MNRAS*, 398, 1601
 Foreman-Mackey, D., Hogg, D. W., Lang, D., & Goodman, J. 2013, *PASP*, 125, 306
 Gagné, J., Mamajek, E. E., Malo, L., et al. 2018, *ApJ*, 856, 23
 Gaia Collaboration 2018, *A&A*, 616, A1
 Gaia Collaboration 2021, *A&A*, 649, A1
 Gardner, J. P., Mather, J. C., Clampin, M., et al. 2006, *SSRv*, 123, 485
 Gauza, B., Béjar, V. J. S., Pérez-Garrido, A., et al. 2015, *ApJ*, 804, 96
 Girard, J. H., Leisenring, J., Kammerer, J., et al. 2022, *Proc. SPIE*, 12180, 121803Q
 Gonzales, E. C., Burningham, B., Faherty, J. K., et al. 2021, *ApJ*, 923, 19
 Gravity Collaboration, Lacour, S., Nowak, M., et al. 2019, *A&A*, 623, L11
 Harris, C. R., Millman, K. J., van der Walt, S. J., et al. 2020, *Natur*, 585, 357
 Hinkley, S., Carter, A. L., Ray, S., et al. 2022, *PASP*, 134, 095003
 Hinkley, S., Lacour, S., Marleau, G. D., et al. 2023, *A&A*, 671, L5
 Høg, E., Fabricius, C., Makarov, V. V., et al. 2000, *A&A*, 355, L27

- Hogg, D. W., Myers, A. D., & Bovy, J. 2010, *ApJ*, **725**, 2166
- Hunter, J. D. 2007, *CSE*, **9**, 90
- Ishihara, D., Onaka, T., Kataza, H., et al. 2010, *A&A*, **514**, A1
- Kammerer, J., Girard, J., Carter, A. L., et al. 2022, *Proc. SPIE*, **12180**, 121803N
- Karalidi, T., Marley, M., Fortney, J. J., et al. 2021, *ApJ*, **923**, 269
- Keppler, M., Benisty, M., Müller, A., et al. 2018, *A&A*, **617**, A44
- Krist, J. E., Balasubramanian, K., Beichman, C. A., et al. 2009, *Proc. SPIE*, **7440**, 74400W
- Krist, J. E., Balasubramanian, K., Muller, R. E., et al. 2010, *Proc. SPIE*, **7731**, 77313J
- Lacour, S., Wang, J. J., Nowak, M., et al. 2020, *Proc. SPIE*, **11446**, 1144600
- Lacour, S., Wang, J. J., Rodet, L., et al. 2021, *A&A*, **654**, L2
- Lafrenière, D., Marois, C., Doyon, R., Nadeau, D., & Artigau, É. 2007, *ApJ*, **660**, 770
- Lajoie, C.-P., Soummer, R., Pueyo, L., et al. 2016, *Proc. SPIE*, **9904**, 99045K
- Linder, E. F., Mordasini, C., Mollière, P., et al. 2019, *A&A*, **623**, A85
- Liu, M. C. 2004, *Sci*, **305**, 1442
- Macintosh, B., Graham, J. R., Ingraham, P., et al. 2014, *PNAS*, **111**, 12661
- Males, J. R., Close, L. M., Müller, K., et al. 2018, *Proc. SPIE*, **10703**, 1070309
- Marleau, G.-D., Coleman, G. A. L., Leleu, A., & Mordasini, C. 2019, *A&A*, **624**, A20
- Marleau, G. D., & Cumming, A. 2014, *MNRAS*, **437**, 1378
- Marley, M. S., Fortney, J. J., Hubickyj, O., Bodenheimer, P., & Lissauer, J. J. 2007, *ApJ*, **655**, 541
- Marley, M. S., Saumon, D., Visscher, C., et al. 2021, *ApJ*, **920**, 85
- Marois, C., Lafrenière, D., Doyon, R., Macintosh, B., & Nadeau, D. 2006, *ApJ*, **641**, 556
- Marois, C., Macintosh, B., Barman, T., et al. 2008, *Sci*, **322**, 1348
- Mawet, D., Milli, J., Wahhaj, Z., et al. 2014, *ApJ*, **792**, 97
- Miles, B. E., Biller, B. A., Patapis, P., et al. 2023, *ApJL*, **946**, L6
- Miles, B. E., Skemer, A. J. I., Morley, C. V., et al. 2020, *AJ*, **160**, 63
- Mollière, P., Molyarova, T., Bitsch, B., et al. 2022, *ApJ*, **934**, 74
- Mollière, P., Stolker, T., Lacour, S., et al. 2020, *A&A*, **640**, A131
- Morley, C. V., Marley, M. S., Fortney, J. J., et al. 2014, *ApJ*, **787**, 78
- Morley, C. V., Skemer, A. J., Miles, B. E., et al. 2019, *ApJL*, **882**, L29
- Müller, M., & Weigelt, G. 1985, *Proc. SPIE*, **556**, 270
- 2020, NASA Exoplanet Science Institute10.26133/NEA12, Planetary Systems Table, IPAC, doi:10.26133/NEA12
- Öberg, K. I., Murray-Clay, R., & Bergin, E. A. 2011, *ApJL*, **743**, L16
- Patapis, P., Nasedkin, E., Cugno, G., et al. 2022, *A&A*, **658**, A72
- Patience, J., King, R. R., De Rosa, R. J., et al. 2012, *A&A*, **540**, A85
- Perrin, M. D., Pueyo, L., Van Gorkom, K., et al. 2018, *Proc. SPIE*, **10698**, 1069809
- Perrin, M. D., Sivaramakrishnan, A., Lajoie, C.-P., et al. 2014, *Proc. SPIE*, **9143**, 91433X
- Perrin, M. D., Soummer, R., & Elliott, E. M. 2012, *Proc. SPIE*, **8442**, 84423D
- Petrus, S., Bonnefoy, M., Chauvin, G., et al. 2020, *A&A*, **633**, A124
- Petrus, S., Bonnefoy, M., Chauvin, G., et al. 2021, *A&A*, **648**, A59
- Phillips, M. W., Tremblin, P., Baraffe, I., et al. 2020, *A&A*, **637**, A38
- Pueyo, L. 2016, *ApJ*, **824**, 117
- Rameau, J., Chauvin, G., Lagrange, A. M., et al. 2013, *ApJL*, **772**, L15
- Ray, S., Hinkley, S., Sallum, S., et al. 2023, *MNRAS*, **519**, 2718
- Rieke, G. H., Wright, G. S., Böker, T., et al. 2015, *PASP*, **127**, 584
- Rieke, M. J., Kelly, D., & Horner, S. 2005, *Proc. SPIE*, **5904**, 1
- Rigby, J., Perrin, M., McElwain, M., et al. 2023, *PASP*, **135**, 048001
- Rodrigo, C., & Solano, E. 2020, in XIV.0 Scientific Meeting (virtual) of the Spanish Astronomical Society, The SVO Filter Profile Service, **182**
- Rodrigo, C., Solano, E., & Bayo, A. 2012, IVOA Working Draft, SVO Filter Profile Service v1.0
- Saumon, D., & Marley, M. S. 2008, *ApJ*, **689**, 1327
- Schlieder, J., Beichman, C. A., Leisenring, J. M., Meyer, M. R., & Ygouf, M. 2017, Survey of Nearby Young M Stars, JWST Proposal. Cycle 1, ID. #1184
- Schwietzman, E. W., Kiang, N. Y., Parenteau, M. N., et al. 2018, *AsBio*, **18**, 663
- Sivaramakrishnan, A., Lafrenière, D., Ford, K. E. S., et al. 2012, *Proc. SPIE*, **8442**, 84422S
- Skilling, J. 2004, in AIP Conf. Ser. 735, Bayesian Inference and Maximum Entropy Methods in Science and Engineering: 24th International Workshop on Bayesian Inference and Maximum Entropy Methods in Science and Engineering, ed. R. Fischer, R. Preuss, & U. V. Toussaint (Melville, NY: AIP), **395**
- Soummer, R., Lajoie, C.-P., Pueyo, L., et al. 2014, *Proc. SPIE*, **9143**, 91433V
- Soummer, R., Pueyo, L., & Larkin, J. 2012, *ApJL*, **755**, L28
- Spiegel, D. S., & Burrows, A. 2012, *ApJ*, **745**, 174
- Sterzik, M. F., Pascucci, I., Apai, D., van der Bliik, N., & Dullemond, C. P. 2004, *A&A*, **427**, 245
- Stolker, T., Marleau, G. D., Cugno, G., et al. 2020a, *A&A*, **644**, A13
- Stolker, T., Quanz, S. P., Todorov, K. O., et al. 2020b, *A&A*, **635**, A182
- 2018, STScI Development Teamsynphot: Synthetic photometry using Astropy, Astrophysics Source Code Library, ascl:1811.001
- Suárez, G., & Metchev, S. 2022, *MNRAS*, **513**, 5701
- Tremblin, P., Amundsen, D. S., Mourier, P., et al. 2015, *ApJL*, **804**, L17
- Van der Walt, S., Schönberger, J. L., Nunez-Iglesias, J., et al. 2014, *PeerJ*, **2**, e453
- van der Walt, S., Schönberger, J. L., Nunez-Iglesias, J., et al. 2014, *PeerJ*, **2**, e453
- Van Rossum, G., & Drake, F. L. 2009, Python 3 Reference Manual (Scotts Valley, CA: CreateSpace)
- Virtanen, P., Gommers, R., Oliphant, T. E., et al. 2020, *NatMe*, **17**, 261
- Wang, J. J., Graham, J. R., Pueyo, L., et al. 2016, *AJ*, **152**, 97
- Wang, J. J., Kulikaukas, M., & Blunt, S. 2021, whereistheplanet: Predicting positions of directly imaged companions, Astrophysics Source Code Library, ascl:2101.003
- Wang, J. J., Ruffio, J.-B., De Rosa, R. J., et al. 2015, pyKLIP: PSF Subtraction for Exoplanets and Disks, Astrophysics Source Code, record ascl:1506.001
- Weinberger, A. J., Becklin, E. E., Schneider, G., et al. 1999, *ApJL*, **525**, L53
- Wells, M., Pel, J. W., Glasse, A., et al. 2015, *PASP*, **127**, 646
- Witte, S., Helling, C., & Hauschildt, P. H. 2009, *A&A*, **506**, 1367
- Wright, E. L., Eisenhardt, P. R. M., Mainzer, A. K., et al. 2010, *AJ*, **140**, 1868
- Yelverton, B., Kennedy, G. M., Su, K. Y. L., & Wyatt, M. C. 2019, *MNRAS*, **488**, 3588
- Ygouf, M., Beichman, C. A., De Furio, M., et al. 2021, Demonstrating a Model-based Coronagraphic Phase Retrieval for Processing of High-Contrast-Imaging Observations with the James Webb Space Telescope, JWST Proposal. Cycle 1, ID. #2627
- Zahnle, K. J., & Marley, M. S. 2014, *ApJ*, **797**, 41
- Zhang, Y., Snellen, I. A. G., & Mollière, P. 2021, *A&A*, **656**, A76